ANNUAL REVIEWS

Annual Review of Physical Chemistry

Spectroscopy in Nanoscopic Cavities: Models and Recent Experiments

Marc R. Bourgeois,[1] Feng Pan,[2] C. Praise Anyanwu,[1] Austin G. Nixon,[1] Elliot K. Beutler,[1] Jennifer A. Dionne,[2,3] Randall H. Goldsmith,[4] and David J. Masiello[1]

[1]Department of Chemistry, University of Washington, Seattle, Washington, USA; email: masiello@uw.edu

[2]Department of Materials Science and Engineering, Stanford University, Stanford, California, USA

[3]Department of Radiology, Stanford University, Stanford, California, USA

[4]Department of Chemistry, University of Wisconsin–Madison, Madison, Wisconsin, USA

Annu. Rev. Phys. Chem. 2024. 75:509–34

The *Annual Review of Physical Chemistry* is online at physchem.annualreviews.org

https://doi.org/10.1146/annurev-physchem-083122-125525

Keywords

optical spectroscopy, electron beam spectroscopy, nanophotonic cavities, weak coupling, strong coupling, ultrastrong coupling

Abstract

The ability of nanophotonic cavities to confine and store light to nanoscale dimensions has important implications for enhancing molecular, excitonic, phononic, and plasmonic optical responses. Spectroscopic signatures of processes that are ordinarily exceedingly weak such as pure absorption and Raman scattering have been brought to the single-particle limit of detection, while new emergent polaritonic states of optical matter have been realized through coupling material and photonic cavity degrees of freedom across a wide range of experimentally accessible interaction strengths. In this review, we discuss both optical and electron beam spectroscopies of cavity-coupled material systems in weak, strong, and ultrastrong coupling regimes, providing a theoretical basis for understanding the physics inherent to each while highlighting recent experimental advances and exciting future directions.

1. INTRODUCTION

EMLDOS: electromagnetic local density of states, counting the number of electromagnetic states per unit volume per unit frequency

Environmental boundaries can strongly influence otherwise unremarkable free-space wave behavior, leading to unexpected and even exceptional wave phenomena. Acoustic whispering galleries in domed architectural structures (1), efficient radio-frequency surface wave propagation near the Earth's surface (2), optical cloaking in metamaterials (3, 4), and even corralling (5) and scarring (6) of quantum matter waves represent just a few examples spanning acoustic, electromagnetic, and quantum realms.

As reported originally in 1966, Drexhage experimentally examined the important situation of a molecular dye (a europium dibenzoylmethane complex) positioned in the vicinity of a gold interface, acting as a mirror boundary for the molecule's fluorescent emission (7, 8). When excited, the dye's radiation was reflected from the gold mirror, subsequently interfering against its own nonreflected emission and resulting in observed modifications to the dye's free-space angular radiation profile and lifetime. Intuitive arguments based on path length differences between the nonreflected and reflected emission components were later quantitatively shored up in the theoretical work of Kuhn (9) and summarized in the famous review by Chance, Prock, and Silbey (10), in which the dye's lifetime and resonance frequency modifications were made explicit through the use of a damped-driven oscillator model incorporating the reflected field set up by the specific boundary conditions of the gold mirror.

Today we understand Drexhage's experiments—like Purcell's earlier description of the enhancement of spontaneous emission of nuclear magnetic moment transitions coupled to a resonant electrical circuit (11)—to be fundamentally governed by the increase in the electromagnetic local density of states (EMLDOS), ρ, induced by the environment over that occurring in free space, $\rho_0 = \omega^2/\pi^2 c^3$. (Gaussian units are used throughout, and dimensions of all important quantities are provided in the **Supplemental Material**.) Essentially all radiative processes in which emitters interact with modified electromagnetic environments can also be explained by modification of ρ/ρ_0. Surface-enhanced Raman scattering (SERS), surface-enhanced fluorescence, and scanning near-field optical microscopy represent three notable examples that take advantage of the remarkable ability of surface plasmon resonances, occurring in metallic nanocavities (12, 13), to modify the EMLDOS through their efficient coupling of free-space radiation to the near-field. In addition to metallic cavities, a diverse range of dielectric microcavities (14), including whispering gallery mode (WGM) microresonators (15) (e.g., microtoroid, microsphere, and microbubble platforms), Fabry-Pérot interferometers (16), and photonic crystals (17–19), may be viewed as receptacles for light with high quality (Q) factors, capable of trapping and storing electromagnetic waves for exceedingly long times (~100 ns), thereby providing substantial EMLDOS modification capabilities. This review will examine recent experiments in which photonic cavities are utilized to detect and spectroscopically characterize a broad range of molecular, solid-state, and nanophotonic systems.

Supplemental Material >

Prominent in each of these examples are the central role and influence of the environment upon the system. Such processes operate in a regime of weak coupling, whereby the rate of energy lost to the environment exceeds the rate of energy transferred between system components. In such cases, the environment serves as a perturbatively connected reservoir, but the original basis characterizing the system remains the physically relevant basis of description. As a result, spectroscopic features of the perturbed system are qualitatively reminiscent of the free system in empty space.

In the opposite regime lie physical systems that are so well isolated that environmental coupling can be completely ignored and only coherent energy exchange between different system components is of importance. In this so-called strong coupling regime, spectroscopic signatures of the system no longer resemble those of its original uncoupled states, and the appropriate representation is that of mixed or normal modes such as the familiar in-phase and out-of-phase oscillations

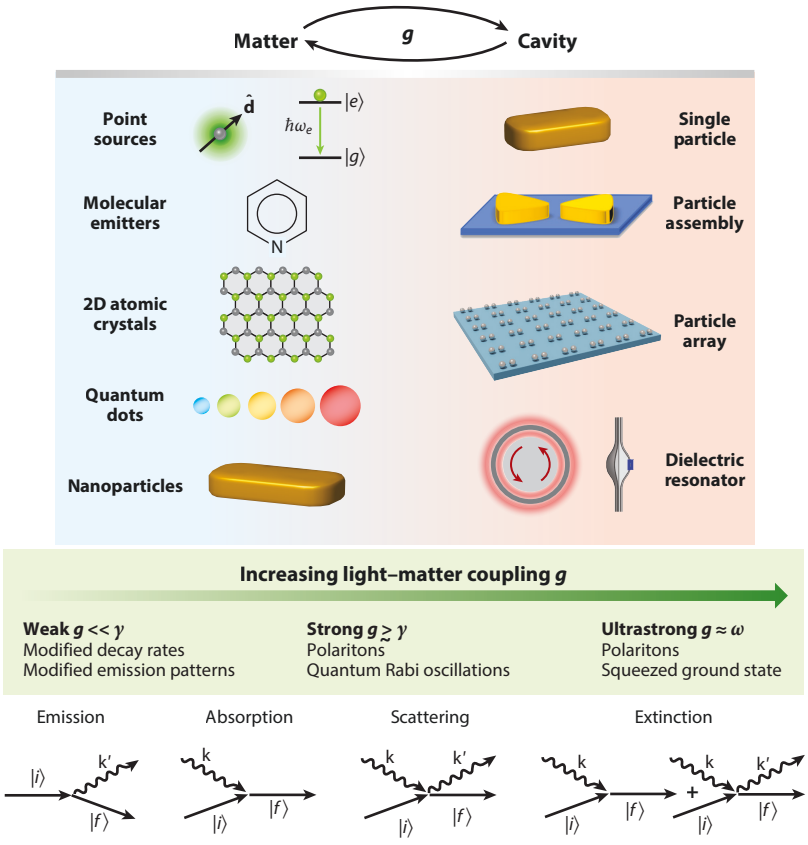

Figure 1

Overview of coupled light–matter degrees of freedom involving atomic, molecular, excitonic, plasmonic, and phononic material components interacting with individual, composite, and structured nanophotonic cavity environments. The degree of light–matter coupling (g) relative to loss (γ) dictates the observed physical characteristics of each system. Displayed at the bottom are diagrammatic representations of familiar light–matter interaction processes which may be probed using both far-field and near-field optical and electron beam sources. The sinusoidal arrows represent photons of wavevectors $\mathbf{k}$ and $\mathbf{k}'$, while the straight arrows represent initial and final material states labeled by $|i\rangle$ and $|f\rangle$, respectively.

of a pair of coupled oscillators. Such strongly coupled systems can occur in many different ways, blended in matter–matter, matter–light, or light–light combinations and realized, for example, in coupled plasmonic nanostructures composed of noble metal nanoparticles, solid-state exciton polaritons formed through the hybridization of 2D transition metal dichalcogenides and nanophotonic cavities, or photonic molecules constructed in exquisitely engineered assemblies of optical resonators, respectively. In some cases, experimental knobs exist to actively tune the degree of mode mixing, while in exceptional situations there exists so much control that strongly coupled systems can even be driven into the weak coupling regime and back again, such as in tip-enhanced photoluminescence (TEPL) measurements.

In this review, we focus on spectroscopic observations of weakly and strongly coupled plasmonic, excitonic, molecular, and nanophotonic systems reported in the recent literature (**Figure 1**). Spectroscopic observables of relevance herein include both near-field [TEPL, nanoscale Fourier transform infrared (nano-FTIR)] and far-field (absorption, SERS) optical

measurements as well as those based upon the inelastic scattering of focused electron beams, such as electron energy loss (EEL), electron energy gain (EEG), and cathodoluminescence (CL) spectroscopies performed in an electron microscope. Specifically, we do not discuss molecular vibrational polariton chemistry and only briefly describe spectroscopic observations of systems characterized by ultrastrong coupling, where the intrasystem coupling rate approaches that of the natural frequencies of the individual system components themselves.

Broadly, this review is divided into two main sections on weak and strong coupling, and emphasis is placed on the introduction of simple theoretical models that (*a*) capture the most salient characteristics encoded within experimental observables, (*b*) provide insights on how nanophotonic cavities work to modify emission rates, and (*c*) serve as a basis for more sophisticated treatments and future research directions. It is our hope that beginning graduate students and advanced researchers who are interested in learning a new field will find this review useful as a first step into the recent literature and in understanding the basic concepts upon which it depends.

2. WEAKLY COUPLED SYSTEMS

The rate at which energy is lost from a physical system to its environment can be due to a myriad of different radiative and nonradiative mechanisms and pathways. The weak coupling regime is distinguished by the situation in which the rate of system–environmental coupling (γ) exceeds that of intrasystem coupling (g). In this regime, different system components merely dress each other as energy flows from one component to another, only to be immediately outcoupled to the environment and forever lost. Here, perturbation theory serves as an effective calculation tool. However, gone are the familiar Hermitian Hamiltonians and their unitary time evolution: Description of such open systems requires Hamiltonians that are fundamentally non-Hermitian in character (20, 21).

Numerous important spectroscopic phenomena in micro and nanoscopic cavities are well characterized as occurring in the weak coupling regime. Examples include: (*a*) the Purcell effect, whereby the rate of spontaneous emission of a quantum emitter to the radiation field can be influenced by its coupling to a mode of an optical or plasmonic cavity in/on which it is located (22–27); (*b*) the plasmonic Fano effect, in which a spectrally narrow plasmonic mode is weakly coupled to and receives energy from another that is significantly lossier (28–34), leading to pronounced asymmetric resonance lineshapes or "cut-outs" in the composite system spectrum; and (*c*) SERS, wherein the exceedingly small cross section for inelastic light scattering by a molecular system is increased due to coupling of the incident laser and scattered molecular fields to the strong antenna-like resonances of a nearby plasmonic nanostructure (35–39).

Many other notable examples of cavity-modified spectroscopic phenomena exist in the literature, but here we focus primarily on the Fano, Purcell, and SERS effects; specific discussion of these effects appears below in Sections 2.1, 2.4, and 2.5, respectively. Generic to such phenomena are the following set of Newton equations, which may be derived either classically or quantum mechanically, representing a weakly coupled emitter–cavity system (31),

$$\begin{aligned} m\ddot{q}_e + m\gamma_e^{\mathrm{nr}}\dot{q}_e + m\omega_e^2 q_e - g_{pq}(\mathbf{s})\sqrt{\frac{m}{V}}\dot{q}_c &= -eE_0 e^{-i\omega t} + \frac{2e^2}{3c^3}\dddot{q}_e, \\ \frac{1}{V}\ddot{q}_c + \frac{1}{V}\gamma_c^{\mathrm{tot}}(\omega)\dot{q}_c + \frac{1}{V}\omega_c^2 q_c + g_{pq}(\mathbf{s})\sqrt{\frac{m}{V}}\dot{q}_e &= 0, \end{aligned} \qquad 1.$$

with coupling strength $g_{pq}(\mathbf{s}) = -e\sqrt{4\pi/mV}\,\mathbf{f}(\mathbf{s})\cdot\hat{\mathbf{q}}_e$. Here, q_e ($\mathbf{q}_e = \hat{\mathbf{q}}_e q_e$) is the emitter's dynamical coordinate with effective mass m, nonradiative decay rate γ_e^{nr}, and natural frequency ω_e, and q_c is the cavity's dynamical coordinate of mode volume V, spatial mode profile $\mathbf{f}(\mathbf{x})$, total (nonradiative

+ radiative) decay rate $\gamma_c^{\mathrm{tot}}(\omega)$, and natural frequency ω_c. Treatment of lossy cavities necessitates a more nuanced description in which the mode functions $\mathbf{f}(\mathbf{x})$ become quasinormal modes with associated complex-valued eigenfrequencies (40–46). The emitter, located at the position $\mathbf{s}$ within the cavity field $\mathbf{E}(\mathbf{x},t) = -(\sqrt{4\pi}/V)\mathbf{f}(\mathbf{x})\dot{q}_c(t)$, is coupled to a harmonic driving field E_0 and to the free radiation field via the radiation reaction force $F_{\mathrm{rad}} = (2e^2/3c^3)\dddot{q}_e = -m\gamma_e^{\mathrm{rad}}(\omega)\dot{q}_e$, with radiative decay rate $\gamma_e^{\mathrm{rad}}(\omega) = 2e^2\omega^2/3mc^3 = (2\pi^2e^2/3m)\rho_0$ (47) expressed in terms of the free-space EMLDOS, where $-e$ is the elementary charge and c is the speed of light.

For multimode cavities, the mode functions $\mathbf{f}_\ell(\mathbf{x})$ and their associated dynamical coordinates $q_\ell^c(t)$ define the cavity vector potential (in the generalized Coulomb gauge $\nabla \cdot [\varepsilon(\mathbf{x})\mathbf{A}(\mathbf{x})] = 0$) as $\mathbf{A}(\mathbf{x},t) = \sum_\ell (\sqrt{4\pi}c/V_\ell)\mathbf{f}_\ell(\mathbf{x})q_\ell^c(t)$, where the spatial mode functions satisfy the vector Helmholtz equation $\nabla \times \big(\nabla \times \mathbf{f}_\ell(\mathbf{x})\big) = \varepsilon(\mathbf{x})(\omega_\ell^2/c^2)\mathbf{f}_\ell(\mathbf{x})$ on the domain of the cavity described by the piecewise dielectric function $\varepsilon(\mathbf{x})$ with eigenfrequencies ω_ℓ, mode amplitudes $q_\ell^c(t)$, and mode volumes $V_\ell = \int \varepsilon(\mathbf{x})|\mathbf{f}_\ell(\mathbf{x})|^2 d^3x/\max[\varepsilon(\mathbf{x})|\mathbf{f}_\ell(\mathbf{x})|^2]$. In such cases the cavity electric field generalizes accordingly as $\mathbf{E}(\mathbf{x},t) = -\sum_\ell (\sqrt{4\pi}/V_\ell)\mathbf{f}_\ell(\mathbf{x})\dot{q}_\ell^c(t)$, as does the light–matter coupling $g_{pq}(\mathbf{s}) = -e\sum_\ell \sqrt{4\pi/mV_\ell}\mathbf{f}_\ell(\mathbf{s}) \cdot \hat{\mathbf{q}}_e$.

In the simplified case of a single cavity mode coupled weakly to an emitter driven in steady state, the emitter oscillates with the frequency of the driving field $E_0(t) = \mathrm{Re}\{E_0(\omega)e^{-i\omega t}\}$, such that $q_e(t) = \mathrm{Re}\{q_e(\omega)e^{-i\omega t}\}$ with oscillator amplitude

$$
\begin{aligned}
q_e(\omega) &= \frac{-eE_0/m}{\underbrace{\omega_e^2 - \mathrm{Re}\dfrac{g^2\omega^2}{\omega_c^2 - i\omega\gamma_c^{\mathrm{tot}} - \omega^2}}_{\tilde{\omega}_e^2} - i\Big[\underbrace{\omega\gamma_e^{\mathrm{tot}} + \mathrm{Im}\dfrac{g^2\omega^2}{\omega_c^2 - i\omega\gamma_c^{\mathrm{tot}} - \omega^2}}_{\omega\tilde{\gamma}_e}\Big] - \omega^2} \\
&= \underbrace{\frac{-eE_0/m}{\omega_e^2 - i\omega\gamma_e^{\mathrm{tot}} - \omega^2}}_{q_e^0(\omega)} \cdot \frac{\omega_c^2 - i\omega\gamma_c^{\mathrm{tot}} - \omega^2}{\underbrace{\omega_c^2 - \dfrac{g^2\omega^2(\omega_e^2 - \omega^2)}{(\omega_e^2 - \omega^2)^2 + (\omega\gamma_e^{\mathrm{tot}})^2}}_{\tilde{\omega}_c^2} - i\omega\Big[\underbrace{\gamma_c^{\mathrm{tot}} + \dfrac{g^2\omega^2\gamma_e^{\mathrm{tot}}}{(\omega_e^2 - \omega^2)^2 + (\omega\gamma_e^{\mathrm{tot}})^2}}_{\tilde{\gamma}_c}\Big] - \omega^2},
\end{aligned}
\qquad 2.
$$

where $\gamma_e^{\mathrm{tot}}(\omega) = \gamma_e^{\mathrm{nr}} + \gamma_e^{\mathrm{rad}}(\omega)$ is the total decay rate of the emitter. The first form of the emitter's oscillator amplitude shows how its natural resonance frequency $\tilde{\omega}_e(\omega)$ and decay rate $\tilde{\gamma}_e(\omega)$ are modified due to coupling with a cavity. In the weak coupling regime, both $\tilde{\omega}_e(\omega) \approx \tilde{\omega}_e(\omega_e)$ and $\tilde{\gamma}_e(\omega) \approx \tilde{\gamma}_e(\omega_e)$ are well approximated by their values at the free-space emitter frequency ω_e. The second form shows how the emitter's oscillator amplitude can be interpreted as the amplitude of the isolated emitter $q_e^0(\omega)$ multiplied by a factor that depends upon the cavity, which will become useful in the description of Fano antiresonances.

Central to the observation of such weakly coupled light–matter systems are the cross sections for absorption and scattering. Recall that the cross section is given by the ratio of the time-averaged power absorbed or emitted (or scattered) by the emitter relative to the time-averaged incident flux of optical energy, that is, $P/\langle S\rangle$, where $\langle S\rangle = cE_0^2/8\pi$ (47). With the emitter's oscillatory amplitude defined, the time-averaged power for absorption and scattering becomes

$$
\begin{aligned}
P_{\mathrm{abs}}(\omega) &= \frac{\omega}{2\pi}\int_0^{2\pi/\omega} \mathrm{Re}\Big\{-m\gamma_e^{\mathrm{nr}}\dot{q}_e(t)\Big\} \cdot \mathrm{Re}\Big\{\dot{q}_e(t)\Big\}\, dt, \\
P_{\mathrm{scat}}(\omega) &= \frac{\omega}{2\pi}\int_0^{2\pi/\omega} \mathrm{Re}\Big\{-m\gamma_e^{\mathrm{rad}}(\omega)\dot{q}_e(t)\Big\} \cdot \mathrm{Re}\Big\{\dot{q}_e(t)\Big\}\, dt,
\end{aligned}
\qquad 3.
$$

where $2\pi/\omega$ is the period of oscillation. These equations show that the power absorbed or scattered stems from the work performed by the dissipative forces $F_{\mathrm{nr}} = -m\gamma_e^{\mathrm{nr}}\dot{q}_e$ and $F_{\mathrm{rad}} = -m\gamma_e^{\mathrm{rad}}(\omega)\dot{q}_e$ upon the oscillator. It follows that the absorption and scattering cross sections can be expressed as

$$\begin{aligned}\sigma_{\mathrm{abs}}(\omega) &= \frac{4\pi\omega^2}{c}\frac{m}{E_0^2}\gamma_e^{\mathrm{nr}}|q_e(\omega)|^2,\\ \sigma_{\mathrm{scat}}(\omega) &= \frac{4\pi\omega^2}{c}\frac{m}{E_0^2}\gamma_e^{\mathrm{rad}}(\omega)|q_e(\omega)|^2.\end{aligned} \qquad 4.$$

Recognizing that the cavity-dressed emitter's induced dipole moment is defined as $d(\omega) = -eq_e(\omega) = \alpha(\omega)E_0$ implicitly defines the dressed polarizability as

$$\alpha(\omega) = \frac{e^2/m}{\tilde{\omega}_e^2 - i\omega\tilde{\gamma}_e - \omega^2}, \qquad 5.$$

which reduces back to the familiar free-space emitter polarizability $\alpha_0(\omega) = (e^2/m)/(\omega_e^2 - i\omega\gamma_e^{\mathrm{tot}} - \omega^2)$ in the limit $g \to 0$. In this limit, the above cross sections attain their familiar forms (31)

$$\begin{aligned}\sigma_{\mathrm{abs}}(\omega) &= \frac{4\pi\omega}{c}\frac{\gamma_e^{\mathrm{nr}}}{\gamma_e^{\mathrm{tot}}}\mathrm{Im}\,\alpha_0(\omega) = \frac{4\pi\omega}{c}\left(\omega\gamma_e^{\mathrm{nr}}\right)\frac{e^2/m}{(\omega_e^2-\omega^2)^2 + (\omega\gamma_e^{\mathrm{tot}})^2},\\ \sigma_{\mathrm{scat}}(\omega) &= \frac{4\pi\omega}{c}\frac{\gamma_e^{\mathrm{rad}}(\omega)}{\gamma_e^{\mathrm{tot}}}\mathrm{Im}\,\alpha_0(\omega) = \frac{8\pi}{3}\left(\frac{\omega}{c}\right)^4\left|\frac{e^2/m}{\omega_e^2 - i\omega\gamma_e^{\mathrm{tot}} - \omega^2}\right|^2,\end{aligned} \qquad 6.$$

and the sum defines the extinction (total) cross section $\sigma_{\mathrm{ext}}(\omega) = \sigma_{\mathrm{abs}}(\omega) + \sigma_{\mathrm{scat}}(\omega) = (4\pi\omega/c)\mathrm{Im}\,\alpha_0(\omega)$. The absorption cross section is a measure of the amount of incident electromagnetic energy that is dissipated into heat, while the scattering cross section characterizes the amount of incident electromagnetic energy returned to the radiation field.

2.1. Fano Resonance

Relevant to a set of experiments measuring the absorption spectra of individual nano-objects independently from scattering, extinction, and emission is the Fano effect, which was originally observed in the autoionization spectrum of He vapor by Lassettre et al. in 1964 (48). Fano understood the pronounced asymmetric antiresonance lineshapes measured in the spectrum as being due to the interaction of two electronic configurations of He (49)—the discrete $2s2p$ double excitation, which is above the first ionization threshold, and the autoionization continuum. In the following years, such asymmetric lineshapes (now called Fano antiresonances, Fano resonances, or Fano interferences) have been observed in many different physical systems characterized under both optical (29, 31, 50–52) and electron beam (28, 30, 34, 53, 54) probes whenever discrete and continuum channels weakly interact. In such cases, the ratio of the spectrum of the interacting system to the spectrum of the continuum channel can be arranged as $\sigma_{\mathrm{int}}(\omega)/\sigma_{\mathrm{cont}}(\omega) = \left|(\mathcal{Q}+\epsilon)/(\epsilon+i)\right|^2$, where the Fano asymmetry parameter $\mathcal{Q}$ is a frequency-independent number in the vicinity of the antiresonance that can be positive, negative, or zero and completely characterizes the asymmetry of the lineshape, while ϵ is a reduced frequency with respect to the frequency of the discrete mode.

Through appropriate choice of parameters, the pair of coupled oscillator equations in Equation 1 can be used to model the absorption spectra of individual emissive nano-objects coupled, for example, to a nanophotonic resonator cavity, where Fano resonances are observed

whenever the nano-object's linewidth is large in comparison to that of the nanophotonic resonator modes to which it is weakly coupled. With the emitter's total decay rate being large relative to that of the cavity—i.e., $\gamma_e^{\mathrm{tot}} \gg \gamma_c^{\mathrm{tot}}$—and the emitter cavity coupling rate g being less than γ_e^{tot}, the absorption spectrum of the composite emitter–cavity system becomes

$$\begin{aligned}\sigma_{\mathrm{abs}}(\omega) &= \frac{4\pi\omega^2}{c}\frac{m}{E_0^2}\gamma_e^{\mathrm{nr}}|q_e(\omega)|^2 \\ &= \underbrace{\frac{4\pi\omega^2}{c}\frac{m}{E_0^2}\gamma_e^{\mathrm{nr}}|q_e^0(\omega)|^2}_{\sigma_{\mathrm{abs}}^0} \cdot \left|\frac{(\tilde{\omega}_c^2 + i\omega\gamma_c - \omega_c^2)/(\omega\tilde{\gamma}_c) + (\omega^2 - \tilde{\omega}_c^2)/(\omega\tilde{\gamma}_c)}{(\omega^2 - \tilde{\omega}_c^2)/(\omega\tilde{\gamma}_c) + i}\right|^2 \\ &= \sigma_{\mathrm{abs}}^0(\omega) \cdot \left|\frac{\mathcal{Q} + \epsilon}{\epsilon + i}\right|^2, \end{aligned} \qquad 7.$$

where the factor modifying the absorption spectrum $\sigma_{\mathrm{abs}}^0(\omega)$ of the isolated free-space emitter accounts for the fact that the emitter is weakly coupled to a high-Q cavity in addition to the radiation continuum. It is this factor that produces a sharp asymmetric lineshape centered about ω_c or $\epsilon(\omega) = -\mathcal{Q}$, which appears as a "cut-out" (or antiresonance) in the Lorentzian absorption spectrum $\sigma_{\mathrm{abs}}^0(\omega)$ of the emitter. Implicitly defined within Equation 7 are the equations $\epsilon(\omega) = (\omega^2 - \tilde{\omega}_c^2)/\omega\tilde{\gamma}_c$ and $\mathcal{Q}(\omega) = (\tilde{\omega}_c^2 + i\omega\gamma_c - \omega_c^2)/\omega\tilde{\gamma}_c$. In the limit of a lossless cavity we have $\mathcal{Q} \to (\tilde{\omega}_c^2 - \omega_c^2)/\omega\tilde{\gamma}_c$, making explicit the dependence of the Fano lineshape upon detuning. While the latter is a function of frequency, we emphasize that Fano resonances are described only when $\mathcal{Q}$ is constant in the vicinity of the cavity resonance at ω_c. Accurate spectroscopic determination of $\mathcal{Q}$ must be treated with care (29, 31, 50, 51), as, for example, interfering optical pathways occurring in scattering observables may spuriously enhance/suppress spectral asymmetries, making pure absorption measurements ideal for quantification of $\mathcal{Q}$. **Figure 2*a*,*b*** shows examples of Fano antiresonance lineshapes associated with $\mathcal{Q} < 0$, $\mathcal{Q} = 0$, and $\mathcal{Q} > 0$ measured via single-particle absorption spectroscopy.

2.2. Absorption

Absorption measurements of individual nano-objects (nanoparticles or molecules) have been widely reported since the first demonstration of single-molecule absorption at cryogenic temperatures in 1989 (55) and subsequently at room temperature in 2010 (56, 57). Since absorption and scattering cross sections have different dependencies upon target size (absorption and scattering depend linearly and quadratically upon volume, respectively), the absorption spectrum of a small nano-object (in comparison to the wavelength) can be approximated by extinction and obtained by measuring its reflected and/or transmitted power, as its scattering cross section is negligible. However, for larger nano-objects that appreciably scatter, measuring absorption independent of scattering in the far field is challenging.

An indirect measurement based on the photothermal effect leverages photothermally induced changes in a nano-object's local refractive index due to optical excitation (51, 58–62) to provide an avenue to separate absorption from scattering for nano-objects that are large enough to scatter. One class of spectroscopies that takes advantage of such photothermal absorption utilizes optical microresonators as near-field thermometers to measure the absorption of single nanoparticles (29, 31, 50, 51, 63–66) and polymers (67, 68). Using this approach, the absorption spectra of individual gold nanoparticles coupled to a microcavity were systematically investigated (29, 31, 50, 51).

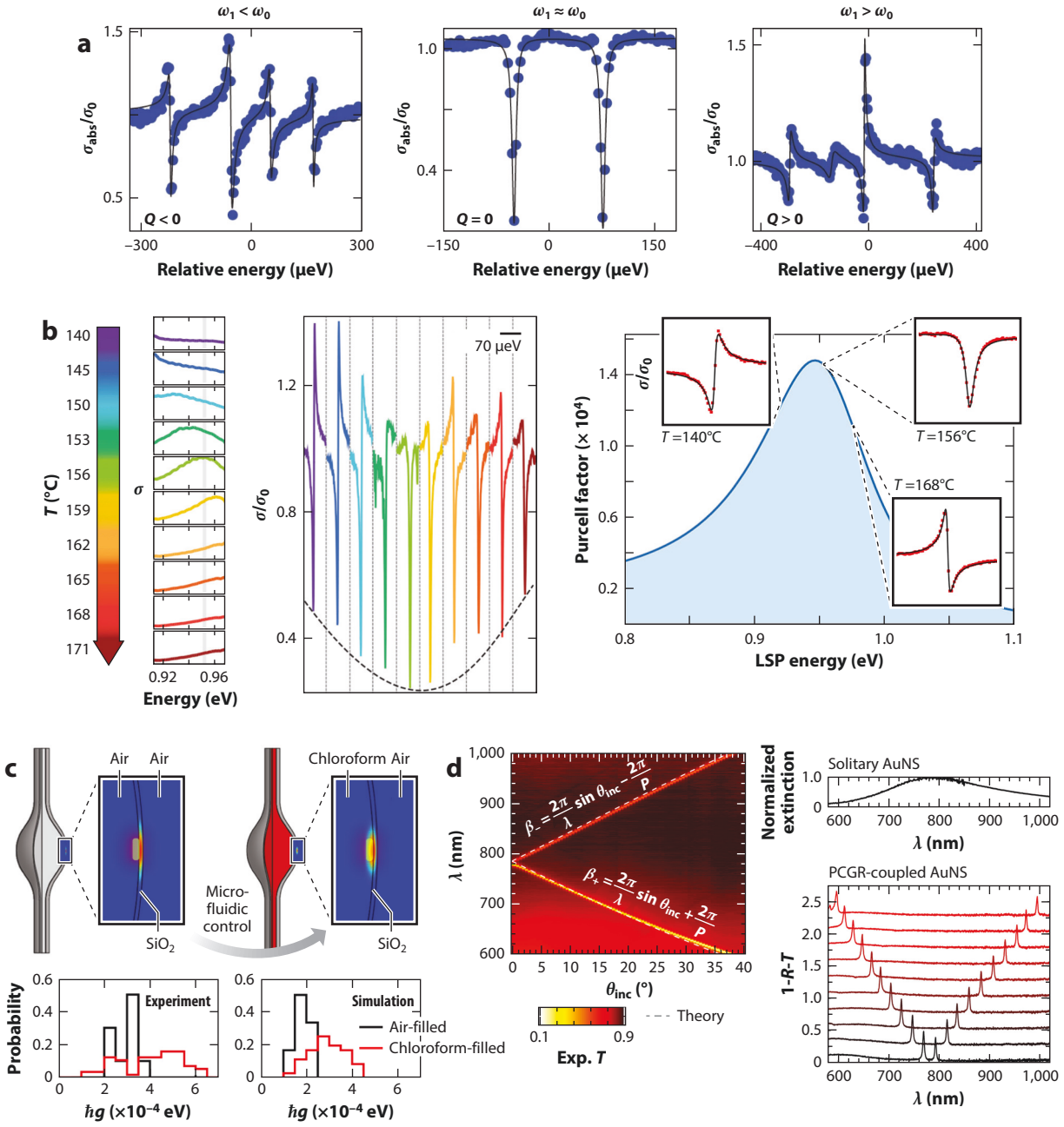

Figure 2

Absorption measurements of plasmonic–photonic coupled systems. (*a*) Fano lineshapes as a function of LSP-WGM detuning. Panel adapted with permission from Reference 51; copyright 2016 Nature. (*b*) Detuning LSP resonance from a single WGM via thermal annealing. Panel adapted with permission from Reference 29; copyright 2017 American Chemical Society. (*c*) Active control of plasmonic–photonic coupling in a microfluidic cavity. Panel adapted with permission from Reference 50; copyright 2022 American Chemical Society. (*d*) Absorption amplification across an extended spectral range through varying the incident angle of excitation. Panel adapted with permission from Reference 69; copyright 2019 American Chemical Society. Abbreviations: AuNS, Au nanostar; LSP, localized surface plasmon; PCGR, photonic crystal–guided resonance; WGM, whispering gallery mode.

In 2016, Heylman et al. employed ultrahigh-quality-factor (Q) WGM toroidal microcavities as single-particle absorption spectrometers to examine single gold nanorods coupled to toroidal microcavities (51). The measured absorption spectra (**Figure 2*a***) were imprinted with distinctive spectral features as a result of the weak coupling between the nanoparticle's lossy dipolar localized surface plasmon (LSP) and the spectrally narrow photonic modes of the microresonator. This led to cavity-modified resonances on top of a broad LSP absorption envelope. Due to the weakly coupled broad LSP mode and quasidiscrete WGM modes, Fano antiresonance signatures with linewidths of a few μeV were observed within the absorption spectrum of each individual gold nanorod (**Figure 2*a***). These Fano signatures manifested as distinctly asymmetric lineshapes with constructive and destructive interference peaks and dips as the LSP-WGM detuning was varied. Subsequently, Thakkar et al. realized a thermal annealing method to control LSP-WGM detunings and consequently sculpt the asymmetry profile of the Fano lineshapes (29), where it was found that the small but finite damping of the resonator's WGM modes was important in the description of the Fano lineshape evolution (**Figure 2*b***). The thermal annealing strategy employed was found to be a facile route to tune the degree of LSP-WGM hybridization and was ultimately used to obtain an optimized Purcell factor of 10^4.

Another way to tune plasmonic-photonic interactions is to directly control LSP-WGM coupling. Pan et al. implemented a WGM microfluidic platform, allowing for control of mode overlap by changing the dielectric environment (50). Specifically, additional WGMs were made accessible to the LSP mode by flowing solvents within the microbubble resonator, thereby creating glass-liquid interfacial modes with better mode overlap (**Figure 2*c***). Huang & Cunningham (69) utilized a direct absorption measurement approach in a different plasmonic-photonic system where absorption dominates over extinction. An absorption enhancement was observed and was continuously tunable across a large spectral range (600–1000 nm), as opposed to the weak absorption measured in uncoupled gold nanostars (69). The Lorentzian peak lineshape was preserved across the uncoupled LSP's absorption range, unlike in LSP-WGM coupled systems. This absorption enhancement was enabled by photonic crystal–guided mode resonances, where the angle-dependent spectral tunability for absorption enhancement follows the photonic crystal–guided mode resonance dispersion (**Figure 2*d***).

2.3. Reflection, Transmission, and Electron Probes

Plasmonic-photonic coupled systems can also be interrogated through tapered optical fiber transmission (31, 70) or (free-space or fiber) reflection measurements (71–74). In a coupled LSP-WGM system, Ruesink et al. observed a blue shift in the measured transmission resonance through a tapered optical fiber as the pitch size in an array of nanoantennas decreased (70). Such strong resonance shifts perturbed by the nanoantennas, which exceeded the effects exerted by the nanoantenna's polarizability, were attributed to a nontrivial phase relationship between the WGM cavity and LSP radiation (**Figure 3*a***). In a similar system, the authors measured specular reflection from the array of nanoantennas coupled to a WGM cavity through a high–numerical aperture objective while changing the incident angle (72). The resonance lineshapes in the reflection spectra were found to vary drastically as the in-plane k-vector increased. These measurements suggest that nanoantenna polarizability can be controlled through backaction via a single cavity mode for the entire nanoantennna array (**Figure 3*b***). Recently, the authors showed the ability to obtain fiber reflection, transmission, and free-space scattering simultaneously by driving the coupled system with a narrow-band tunable laser through a tapered optical fiber (73, 74). Single plasmonic nanoparticles were deterministically positioned on WGM microcavities through electron beam lithography. A perturbed cavity mode with a broader lineshape than that for the unperturbed cavity mode suggested LSP-WGM hybridization, which was further confirmed by scattering images.

Pan et al. demonstrated simultaneous measurement of absorption and transmission through a single tapered optical fiber to elucidate energy pathways in a weakly coupled LSP-WGM system (31) (**Figure 3*c***). Through a combination of experimental measurement and theoretical modeling, key system parameters were found to span across 9 orders of magnitude, including LSP and WGM nonradiative and radiative dissipation rates and their mutual coupling strength.

Beyond these optical measurements, there are several recent demonstrations (30, 75, 76) in which electrons were used to probe weakly coupled systems using an electron microscope. Smith et al. combined EEL spectroscopy and theoretical modeling to reveal infrared plasmonic Fano

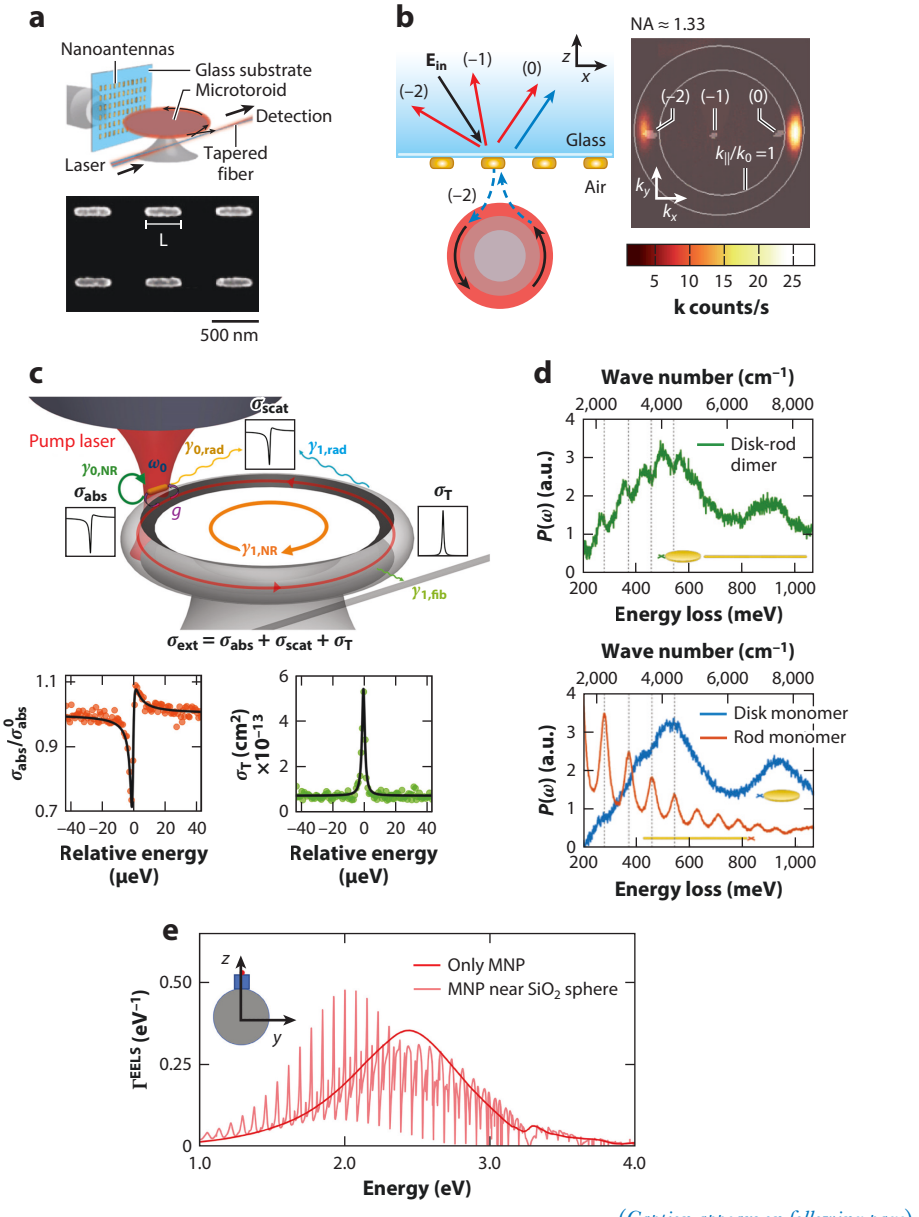

(*Caption appears on following page*)

Figure 3 (*Figure appears on preceding page*)

Reflection, transmission, and electron probes. (*a*) Transmission measurement of a WGM microcavity coupled to an array of gold nanoparticles through a tapered optical fiber. Panel adapted with permission from Reference 70; copyright 2015 American Physical Society. (*b*) Addressing the LSP-WGM coupled system through back-focal-plane reflection imaging. Panel adapted with permission from Reference 72; copyright 2018 American Physical Society. (*c*) Simultaneous measurement of absorption and two-sided transmission of a plasmonic–photonic coupled cavity. Panel adapted with permission from Reference 31; copyright 2019 American Chemical Society; (*d*) EEL spectroscopy of a disk-rod dimer consisting of gold nanodisk and microrod (*left*) and their components (*right*). Panel adapted with permission from Reference 30; copyright 2019 American Physical Society. (*e*) EEL spectroscopy of a silver nanocube coupled to a WGM glass microsphere. Panel adapted with permission from Reference 75; copyright 2021 American Chemical Society. Abbreviations: EEL, electron energy loss; LSP, localized surface plasmon; MNP, metallic nanoparticle; WGM, whispering gallery mode.

antiresonances in a gold disk–rod dimer system (**Figure 3*d***) due to the coupling between quasidiscrete Fabry-Pérot modes in the gold rod and the quasicontinuum LSP mode in the gold disk (30). In a nanocube-microsphere coupled system (**Figure 3*e***), EEL spectroscopy and CL were used to examine the broad LSP resonance in a silver nanocube modulated by discrete WGMs (75). Interestingly, the excitation of WGMs with transverse-magnetic and/or transverse-electric polarization was controlled by changing the electron probe position on the nanocube.

2.4. Purcell Enhancement

Since Purcell's original report in 1946 of the ability to modify spontaneous emission rates beyond their vacuum values (11), numerous physical realizations of cavity-modified emissive processes have appeared in the literature (77). In the context of an emitter coupled weakly to a nanophotonic cavity, the coupled equations of motion (Equation 1) again suffice to describe the cavity-induced modifications to the emitter's radiative decay.

In the absence of a cavity, the power scattered by an isolated emitter (into free space) recovers the well-known Larmor result (47), that is,

$$P^0_{\text{scat}} = \frac{\omega_e}{2\pi}\int_0^{2\pi/\omega_e} \text{Re}\left\{-m\gamma_e^{\text{rad}}(\omega)\dot{q}_e^0(t)\right\}\cdot\text{Re}\left\{\dot{q}_e^0(t)\right\}dt = \frac{\pi^2 e^2\omega_e^2}{3}\rho_0|q_e^0|^2 \qquad 8.$$

for a dipole oscillator oscillating at frequency ω_e, where $\rho_0 = \omega_e^2/\pi^2c^3$ is the free-space EMLDOS. When positioned in a cavity, determination of the modifications to the emitter's dynamics requires calculation of the power scattered by the emitter into the cavity via

$$\begin{aligned} P_{\text{cav}} &= \frac{\omega_e}{2\pi}\int_0^{2\pi/\omega_e} \text{Re}\left\{g_{pq}(\mathbf{s})\sqrt{\frac{m}{V}}\dot{q}_c(t)\right\}\cdot\text{Re}\left\{\dot{q}_e^0(t)\right\}dt \\ &= \frac{2\pi e^2}{V}\frac{\omega_e^4\gamma_c|\mathbf{f}(\mathbf{s})\cdot\hat{\mathbf{q}}_e|^2}{(\omega_c^2-\omega_e^2)^2+(\omega_e\gamma_c)^2}|q_e^0|^2 \\ &= \frac{2\pi^3 e^2c^3}{V}\frac{\omega_e^2\gamma_c|\mathbf{f}(\mathbf{s})\cdot\hat{\mathbf{q}}_e|^2}{(\omega_c^2-\omega_e^2)^2+(\omega_e\gamma_c)^2}\rho_0|q_e^0|^2, \end{aligned} \qquad 9.$$

where both the emitter and cavity modes oscillate in time as $e^{-i\omega_e t}$, so that the ratio

$$F_P = \frac{P_{\text{cav}}}{P^0_{\text{scat}}} = \frac{6\pi c^3}{V}\frac{\gamma_c|\mathbf{f}(\mathbf{s})\cdot\hat{\mathbf{q}}_e|^2}{(\omega_c^2-\omega_e^2)^2+(\omega_e\gamma_c)^2} \qquad 10.$$

defines the Purcell enhancement factor (EF). If the detuning $(\omega_c - \omega_e)$ is large relative to the cavity decay rate (γ_c), then emission is inhibited. Oppositely, if the cavity is tuned into resonance with

Quality factor: a dimensionless quantity that describes a cavity's temporal decay rate and therefore its ability to localize light in time

the emitter ($\omega_c = \omega_e$), then Purcell enhancement is maximized when the emitter's transition dipole moment is aligned with the cavity field and located at its maximum so that $|\mathbf{f}(\mathbf{s}) \cdot \hat{\mathbf{q}}_e|^2 = 1$. In this case we have

$$F_P = \frac{6\pi c^3}{\omega_e^3}\frac{Q}{V} = \frac{3\lambda_e^3}{4\pi}\frac{Q}{V}, \qquad 11.$$

expressed in terms of the cavity quality factor $Q = \omega_c/\gamma_c$ by rewriting the emitter's resonance frequency as the wavelength $\lambda_e = 2\pi c/\omega_e$. Equation 11 can also be written as

$$F_P = \frac{2Q/\pi\omega_e V}{\omega_e^2/3\pi^2 c^3} = \frac{2Q/\pi\omega_e V}{\rho_0/3}, \qquad 12.$$

where the quantity in the numerator can be thought of as the cavity-enhanced density of electromagnetic states $\rho = 2Q/\pi\omega_e V$, providing a new interpretation of the physical origin of the Purcell EF.

2.5. Surface-Enhanced Raman Scattering

Raman scattering is a second-order, instantaneous two-photon inelastic scattering process whereby molecular analytes annihilate an incoming photon at frequency ω and emit an outgoing photon at frequency ω'. Processes involving emitted photons with energy below (above) that of the incoming photon are referred to as Stokes (anti-Stokes) scattering (**Figure 4*a*,*b***), and

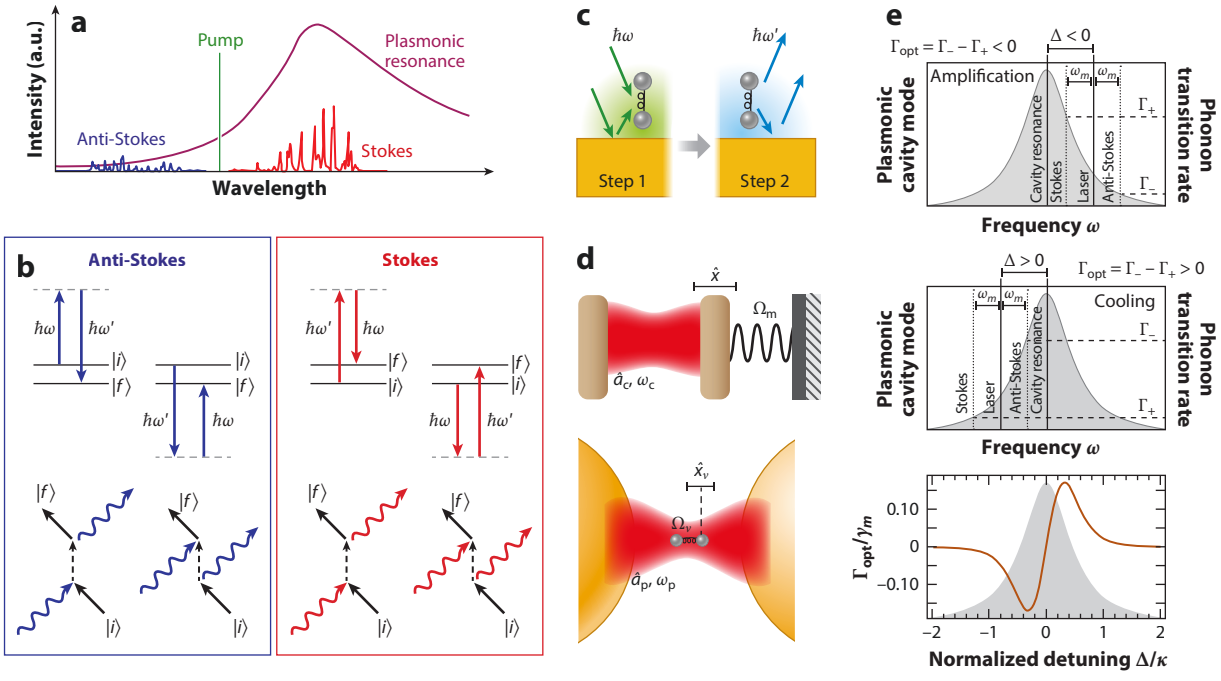

Figure 4

Surface-enhanced Raman scattering (SERS). (*a*) Example SERS spectrum. (*b*) Feynman diagrams for Stokes and anti-Stokes scatterings along with their respective level scheme depictions. (*c*) Two-step phenomenological description of SERS. (*d*) Optomechanical model of SERS. Panel adapted with permission from Reference 83; copyright 2016 Springer Nature. (*e*) The cavity-laser drive detuning Δ dictates whether amplification ($\Gamma_{opt} < 0$) or cooling ($\Gamma_{opt} > 0$) of molecular vibrations occurs within the optomechanical model. Panel adapted with permission from Reference 84; copyright 2017 Royal Society of Chemistry.

energy differences $\hbar\omega_R = |\hbar\omega - \hbar\omega'|$ must be equal to the energy difference between initial and final internal (often vibrational) molecular states. Although the molecular vibrational spectra accessed by Raman scattering encode detailed molecular structure information, Raman signals are generally quite low—for example, the Raman scattering cross section for pyridine is $\sigma \sim 10^{-30}$ cm^2. However, enormous enhancement in measured Raman scattering of analytes in the presence of metal substrates with nanoscale features was observed in 1974 (78) and independently in 1977 (37, 79), with the proper interpretation based on excitation of resonant surface modes beginning shortly thereafter (80). Today, SERS EFs of $\gtrsim 10^{8-12}$, variably defined (81) but generally a ratio of scattered powers in the presence/absence of a nanophotonic cavity, are routinely achievable with carefully designed nanocavity systems, allowing vibrational spectra of individual molecules to be recorded with single-molecule SERS (38, 39). While imperfect, the overall SERS EF is conventionally decomposed into electromagnetic enahncement (EME) and chemical enhancement (CE) contributions, with (total EF) = (EME) · (CE). CE mechanisms involve chemical modification of molecular vibrational characteristics via interaction with the cavity, for example, due to charge transfer between molecule and substrate, necessitating a detailed microscopic quantum mechanical description (82). This review focuses on the EME mechanism, which arises from the modification of the EMLDOS at the positions of the analyte molecules in the presence of a nanocavity, and is generally the dominant source of SERS enhancement. An expanded discussion of current perspectives on SERS appears in Reference 82.

While many descriptions of SERS have been presented at varying levels of theoretical sophistication—from classical coupled dipole treatments (85) to quantum-mechanical electronic structure methods (86, 87) to many-body theories of coupled molecule–plasmon systems (88)—perhaps the simplest descriptions are those provided by phenomenological models. Although truly an instantaneous second-order scattering process, one such phenomenological description of Raman scattering involves a two-step sequence consisting of induced dipole and reemission steps as depicted in **Figure 4*c*** (81). The presence of a nanophotonic cavity influences each of these steps via its modifications to the EMLDOS. During step one, a Purcell-enhanced Raman dipole moment $\mathbf{d}_R(\omega') = \bar{\boldsymbol{\alpha}}_R \cdot \mathbf{E}(\omega)$ is induced that oscillates at frequency ω'. The Raman polarizability $\bar{\boldsymbol{\alpha}}_R = (\mathbf{Q}_R - \mathbf{Q}_R^0) \cdot \left[\frac{\partial}{\partial \mathbf{Q}_R}\bar{\boldsymbol{\alpha}}(\omega)\right]\Big|_{\mathbf{Q}_R=\mathbf{Q}_R^0}$ is defined through the Taylor expansion of the static polarizability $\bar{\boldsymbol{\alpha}}$, with the vibrational normal mode coordinate $\mathbf{Q}_R$ oscillating around its equilibrium position $\mathbf{Q}_R^0$ at the vibrational frequency ω_R, establishing the relationship $\omega' = \omega \pm \omega_R$.

Treating the Raman dipole and nanocavity as interacting classical dipoles at positions $\mathbf{x}_d$ and $\mathbf{x}_p$, respectively, with $\mathbf{E}_0(\mathbf{x}_d) \approx \mathbf{E}_0(\mathbf{x}_p) \equiv \mathbf{E}_0$, we have

$$\mathbf{d}_R = \bar{\boldsymbol{\alpha}}_R \cdot (\mathbf{E}_0 + \bar{\mathbf{G}}_{dp} \cdot \bar{\boldsymbol{\alpha}}_p \cdot \mathbf{E}_0) = \bar{\boldsymbol{\alpha}}_R \cdot \left[\bar{\mathbf{I}} + \bar{\mathbf{M}}_{\text{loc}}(\omega)\right] \cdot \mathbf{E}_0, \qquad 13.$$

where $\bar{\mathbf{M}}_{\text{loc}}(\omega) = \bar{\mathbf{G}}_{dp}(\mathbf{x}_d, \mathbf{x}_p, \omega) \cdot \bar{\boldsymbol{\alpha}}_p$ is the local field enhancement tensor at frequency ω determined by the EMLDOS, which enhances (or suppresses) the local field $\mathbf{E}(\mathbf{x}_d) = \bar{\mathbf{G}}_{dp}(\mathbf{x}_d, \mathbf{x}_p, \omega) \cdot \mathbf{p}$ at $\mathbf{x}_d$, and $\mathbf{p}$ is the dipole moment of the laser-driven cavity. Purcell-enhanced emission occurs similarly during the second step, which can be accounted for by considering the total radiated power from the combined Raman–dipole–nanocavity system when sourced by the Raman dipole oscillating at the shifted frequency ω'. Under these conditions, the total dipole moment $\boldsymbol{\mu}_{\text{tot}} = \mathbf{d}_R + \mathbf{p}$ is found to be

$$\boldsymbol{\mu}_{\text{tot}} = \left[\bar{\mathbf{I}} + \bar{\mathbf{M}}_{\text{loc}}(\omega')\right] \cdot \bar{\boldsymbol{\alpha}}_R \cdot \left[\bar{\mathbf{I}} + \bar{\mathbf{M}}_{\text{loc}}(\omega)\right] \cdot \mathbf{E}_0. \qquad 14.$$

Comparing the total power scattered in the presence, $P_{\text{tot}}^{\text{cav}}$, and absence, P_{tot}^0, of the cavity using the Larmor power in Equation 8, it is observed that (*a*) $P_{\text{tot}}^{\text{cav}} \propto |\mathbf{E}_0|^2$, that is, the scattered power

depends linearly on the incident field intensity; and (*b*) the EF is

$$\frac{P_{\text{tot}}^{\text{cav}}}{P_{\text{tot}}^{0}} \sim \frac{|\mathbf{E}(\omega')|^2}{|\mathbf{E}_0(\omega')|^2} \cdot \frac{|\mathbf{E}(\omega)|^2}{|\mathbf{E}_0(\omega)|^2} \sim \frac{|\mathbf{E}(\omega)|^4}{|\mathbf{E}_0(\omega)|^4}, \quad 15.$$

recovering the well-established local field EF with its fourth power dependence upon the local field relative to the applied field when the frequency shift of the emitted light is neglected. It is worth noting that if the Raman and cavity dipoles are allowed to interact self-consistently (85, 88), then the EF is found to be $P_{\text{tot}}^{\text{cav}}/P_{\text{tot}}^{0} = (1 + M_{\text{loc}})^2/(1 - M_{\text{loc}}^2)^2$, within a one-dimensional model for simplicity. This result differs from that of the two-step model only by the presence of the denominator, which is responsible for the classical image dipole effect that renormalizes the cavity and molecular frequencies and lifetimes.

Rotating wave approximation: neglect of the rapidly oscillating interaction picture light–matter coupling terms proportional to $e^{\pm i(\omega_c+\omega_e)t}$

Despite the successes of these single-molecule phenomenological models, they do not provide simple descriptions of other important aspects of SERS, such as nonlinear Stokes and anti-Stokes emission under strong driving and correlations among molecular vibrations. Beginning in 2015, molecular optomechanical models of SERS were introduced, allowing for dynamic interaction between two parametrically coupled, nonresonant harmonic molecular vibrational and cavity oscillators within the framework of cavity quantum electrodynamics (83, 89). In analogy with the above two-step model, the interaction Hamiltonian is

$$\begin{aligned}\hat{H}_{\text{int}} &= -\hat{\mathbf{E}}(\mathbf{x}_d) \cdot \hat{\mathbf{d}}_R \\ &= -\hat{\mathbf{E}}(\mathbf{x}_d) \cdot \frac{1}{2}\left\{(\hat{\mathbf{Q}}_R - \hat{\mathbf{Q}}_R^0) \cdot \left[\frac{\partial}{\partial \mathbf{Q}_R}\tilde{\boldsymbol{\alpha}}(\omega)\right]\Big|_{\mathbf{Q}_R=\mathbf{Q}_R^0} \cdot \hat{\mathbf{E}}(\mathbf{x}_d)\right\} \\ &\approx -g_R\left(\hat{b} + \hat{b}^\dagger\right)\hat{a}^\dagger\hat{a},\end{aligned} \quad 16.$$

where the rotating wave approximation (RWA) has been invoked and the last line involves the introduction of the quantized vibrational coordinate and cavity electric field operators $\hat{\mathbf{Q}}_R - \hat{\mathbf{Q}}_R^0 = \sqrt{\hbar/2m\omega_e}\left(\hat{b}e^{i\phi} + \hat{b}^\dagger e^{-i\phi}\right)$ and $\hat{\mathbf{E}}(\mathbf{x}) = i\sqrt{2\pi\hbar\omega_c/V}\left(\mathbf{f}(\mathbf{x})\hat{a} - \mathbf{f}^*(\mathbf{x})\hat{a}^\dagger\right)$, expressed in terms of the bosonic molecular vibration $\hat{b}$ ($\hat{b}^\dagger$) and cavity $\hat{a}$ ($\hat{a}^\dagger$) lowering (raising) operators, respectively. Together with the additional assumptions that $\mathbf{x}_d$ is positioned at an antinode of the cavity field and is aligned with the local field polarization, the optomechanical coupling is $g_R = \left[\frac{\partial}{\partial \mathbf{Q}_R}\tilde{\boldsymbol{\alpha}}(\omega)\right]\Big|_{\mathbf{Q}_R=\mathbf{Q}_R^0}\sqrt{\hbar/2m\omega_e}(2\pi\hbar\omega_c/V)$ when $\phi = \pi$ is chosen. In the presence of a coherent continuous-wave laser drive at frequency ω_d, the Hamiltonian in the frame rotating at the drive frequency becomes

$$\hat{H} = \hbar\Delta\hat{a}^\dagger\hat{a} + \hbar\omega_c\hat{b}^\dagger\hat{b} - g_R\left(\hat{b} + \hat{b}^\dagger\right)\hat{a}^\dagger\hat{a} + i\hbar\Omega(\hat{a}^\dagger - \hat{a}) \quad 17.$$

in terms of the cavity-drive detuning $\Delta = \omega_c - \omega_d$, where Ω characterizes the strength of driving by the (classical) applied field $E_0(t) = E_0 e^{-i\omega_d t}$.

The molecular optomechanical Hamiltonian is formally equivalent to the well-studied cavity optomechanical Hamiltonian describing a coherently driven Fabry-Pérot cavity with one mirror mounted on a spring (**Figure 4*d***) (90). The dynamics of the open coupled mode system in the presence of incoherent cavity and molecular vibration decay at rates κ and γ_m, respectively, have been investigated using the Langevin (83) as well as master equation (84, 89) approaches. Despite some differences in the expressions for steady-state phonon occupancies, both approaches show that dynamical backaction introduces additional pathways for phonon creation and annihilation characterized by rates Γ_+ and Γ_-, respectively, which can lead to stimulated phonon amplification and cooling. For example, the cavity-mediated phonon creation and annihilation

rates from the master equation approach are

$$\Gamma_{\pm} = \frac{g_0^2 |\alpha|^2 \kappa}{(\Delta \pm \omega_m)^2 + (\kappa/2)^2}, \tag{18.}$$

where α is the coherent state amplitude of the driven cavity mode. The steady-state phonon population at temperature T is

$$n_{ss} = \frac{\gamma_m}{\gamma_m + \Gamma_{opt}} n_{th} + \frac{\Gamma_+}{\gamma_m + \Gamma_{opt}}, \tag{19.}$$

where $\Gamma_{opt} = \Gamma_- - \Gamma_+$, and $n_{th} = [\exp(\hbar\omega_m/k_B T) - 1]^{-1}$ is the thermal phonon occupancy. Inspection of Equation 18 shows that when the laser detuning is such that $\Delta < 0$ ($\Delta > 0$), we have $\Gamma_{opt} < 0$ ($\Gamma_{opt} > 0$), leading to phonon amplification (cooling) as depicted in **Figure 4*e***. Vibrational pumping, therefore, arises naturally within the optomechanical model and leads to the prediction of nonlinear scaling of anti-Stokes SERS with increasing continuous-wave laser excitation, which has been observed in single-molecule SERS measurements within low-temperature picocavities (91). The model also predicts that with still stronger blue-detuned driving (typically beyond what has been experimentally achievable with continuous-wave lasers before the onset of sample damage), we have $\Gamma_{opt} = -\gamma_m$, which causes the phonon population in Equation 19 to diverge and the onset of phonon lasing, which is known as parametric instability. **Figure 5** presents examples from the recent literature that report signatures of collective phenomena in SERS predicted by the optomechanical model (92–94), which are more fully discussed in the **Supplemental Material**.

Supplemental Material >

3. STRONGLY COUPLED SYSTEMS

Just as strong contact of an environment with a physical system is a defining feature of weak coupling, environmental isolation is the hallmark of physical systems in the strong coupling regime. Here, the rate of energy transfer (g) between system components is so large relative to environmental loss (γ) of any form that outcoupling to the environment can be largely neglected. Strongly coupled systems are characterized by repeated and coherent intrasystem energy transfer and are thus described accurately by Hermitian Hamiltonians and unitary time evolution. In the absence of external forces, normal modes (or super modes or molecular orbitals, depending upon the parlance of the particular research community) arise as the natural, independent (i.e., noninteracting) basis on which all driven states of the system including spectra can be decomposed.

Normal modes can vary considerably in their character, ranging from weakly mixed forms that closely resemble the uncoupled system components to maximally mixed, even-weighted superpositions of the original uncoupled system components. In the case of two coordinate-coordinate ($q_1 q_2$) coupled oscillators with Hamiltonian (95)

$$H = \frac{p_1^2}{2m_1} + \frac{1}{2} m_1 \omega_1^2 q_1^2 + \frac{p_1^2}{2m_1} + \frac{1}{2} m_2 \omega_2^2 q_2^2 - g_{qq}(\mathbf{s}) q_1 q_2, \tag{20.}$$

the general forms of the normal mode coordinates and frequencies are

$$\begin{aligned} q_- &= q_1 \left(\frac{m_1}{m_2}\right)^{1/4} \cos\theta + q_2 \left(\frac{m_2}{m_1}\right)^{1/4} \sin\theta, \\ q_+ &= -q_1 \left(\frac{m_1}{m_2}\right)^{1/4} \sin\theta + q_2 \left(\frac{m_2}{m_1}\right)^{1/4} \cos\theta, \end{aligned} \tag{21.}$$

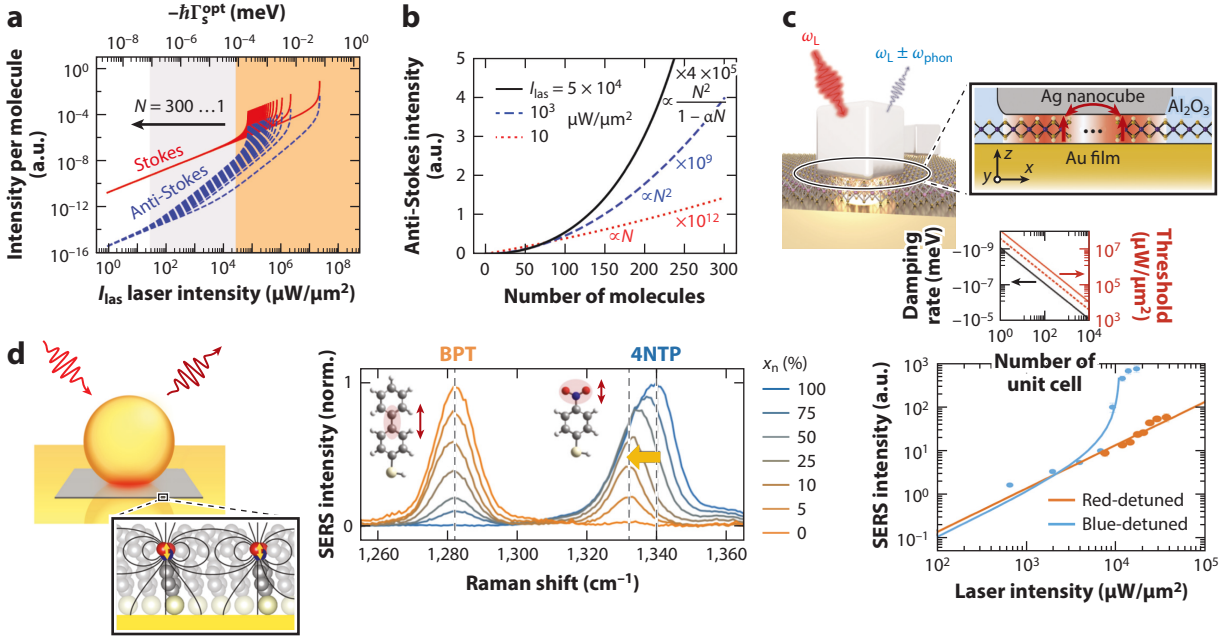

Figure 5

Collective optomechanical effects in SERS. (*a*) Calculated Stokes and anti-Stokes emission intensities as a function of laser intensity and of the number of identical molecules N coupled to the cavity under blue-detuned CW laser drive. Panel adapted with permission from Reference 92; copyright 2020 American Chemical Society. (*b*) Anti-Stokes scattering intensity as a function of N exhibiting quadratic dependence in the vibrational pumping regime (*gray shading* in panel *a*). Panel adapted with permission from Reference 92; copyright 2020 American Chemical Society. (*c*) Measured superlinear Stokes scattered power dependence from monolayer MoS_2 placed within the gap regions of nanocube-on-mirror structures under blue-detuned drive. Panel adapted with permission from Reference 93; copyright 2022 American Chemical Society. (*d*) Intermolecular vibrational coupling between polar bonds on analyte molecules (4NTP) embedded within self-assembled monolayers composed of inert spacer molecules (BPT) leads to a measurable frequency shift detectable in SERS. Panel adapted from Reference 94 (CC BY 4.0). Abbreviations: CW, continuous wave; SERS, surface-enhanced Raman scattering.

$$\omega_- = \sqrt{\omega_1^2 \cos^2\theta + \omega_2^2 \sin^2\theta - \frac{2g_{qq}}{\sqrt{m_1 m_2}} \sin\theta\cos\theta},$$
$$\omega_+ = \sqrt{\omega_1^2 \sin^2\theta + \omega_2^2 \cos^2\theta + \frac{2g_{qq}}{\sqrt{m_1 m_2}} \sin\theta\cos\theta}, \qquad 22.$$

written in terms of the angle $\theta = (1/2)\tan^{-1} 2g_{qq}/\sqrt{m_1 m_2}(\omega_2^2 - \omega_1^2)$ dictating the degree of mode mixing experienced between the coupled coordinates q_1 and q_2. At zero detuning, the energetic splitting between the normal modes is $\hbar\sqrt{2g/\sqrt{m_1 m_2}}$. Such equations might, for example, describe two coupled plasmonic nanoparticles with dipolar coordinates $\mathbf{d}_1 = -e\hat{\mathbf{q}}_1 q_1$ and $\mathbf{d}_2 = -e\hat{\mathbf{q}}_2 q_2$ and coupling strength $g_{qq}(\mathbf{s}) = e^2 \hat{\mathbf{q}}_1 \cdot \mathbf{G}(\mathbf{s}) \cdot \hat{\mathbf{q}}_2$ derived from the interaction energy $H_{int} = -\mathbf{E}_1(\mathbf{s}) \cdot \mathbf{d}_2 = -\mathbf{d}_1 \cdot \mathbf{E}_2(-\mathbf{s}) = -\mathbf{d}_1 \cdot \mathbf{G}(\mathbf{s}) \cdot \mathbf{d}_2 = -g_{qq}(\mathbf{s}) q_1 q_2$, where

$$\mathbf{G}(\mathbf{s}) = \left[(3\hat{\mathbf{s}}\hat{\mathbf{s}} - 1)\left(\frac{1}{s^3} - \frac{ik}{s^2}\right) - (\hat{\mathbf{s}}\hat{\mathbf{s}} - 1)\frac{k^2}{s}\right] e^{iks} \qquad 23.$$

is the free-space dipole relay tensor (47), with $k = \omega/c$ relaying the electric field $\mathbf{E}(\mathbf{s}) = \mathbf{G}(\mathbf{s}) \cdot \mathbf{d}$ produced by one dipole to the other located at the position $\mathbf{s} = \hat{\mathbf{s}}s$ away. The effective mass m_i of each plasmonic dipole mode ($i = 1, 2$) (96, 97) can be derived from the Clausius-Mossotti polarizability together with a Drude model of the nanoparticle's bulk free carrier response. This

dipolar coupling scheme as well as other more sophisticated couplings can all be derived from the exact minimal coupling formalism (98).

Other strongly coupled light–matter and light–light systems are governed by similar Hamiltonians with a few replacements. For massless light modes, such as the optical eigenmodes of nanophotonic cavities, the effective mass m is replaced by the inverse mode volume V. Additionally, the form of the interaction energy changes to coordinate-momentum (q_1p_2) coupling for interacting light–matter systems (29, 31, 50, 51) and to doubly coupled coordinate-coordinate (q_1q_2) and momentum-momentum (p_1p_2) couplings for interacting light–light systems (99, 100).

Polaritons: the emergent collective excitations of strongly coupled light–matter degrees of freedom

Interacting light–matter Hamiltonians arise, for example, in the description of high-quality (Q) nanophotonic cavity coupled atomic, molecular, excitonic, or plasmonic degrees of freedom blended into new hybrid states called polaritons. In general, polaritons are the collective excitations that emerge in the hybridization of optical and material degrees of freedom and can be engineered to vary in their degree of mode mixing, in analogy to Equation 21, by exerting control over parameters such as detuning and coupling strength. Given the light–matter interaction energy $H_{\text{int}} = -\mathbf{E}(\mathbf{s}) \cdot \mathbf{d}$, with cavity electric field $\mathbf{E} = -\dot{\mathbf{A}}/c$ and cavity magnetic field $\mathbf{B} = \nabla \times \mathbf{A}$, the light-matter Hamiltonian becomes (31)

$$\begin{aligned} H &= \int \frac{\mathbf{E}^2 + \mathbf{B}^2}{8\pi} d^3x + \frac{p_e^2}{2m} + \frac{1}{2} m\omega_e^2 q_e^2 - \mathbf{E}(\mathbf{s}) \cdot \mathbf{d} \\ &= \frac{V p_c^2}{2} + \frac{1}{2V} \omega_c^2 q_c^2 + \frac{p_e^2}{2m} + \frac{1}{2} m\omega_e^2 q_e^2 - \sqrt{mV}\, g_{pq}(\mathbf{s}) p_c q_e \end{aligned} \qquad 24.$$

in the case of one nanophotonic cavity mode $\mathbf{A}(\mathbf{x}, t) = (\sqrt{4\pi}c/V)\mathbf{f}(\mathbf{x})q_c(t)$ of frequency ω_c, volume V, spatial mode profile $\mathbf{f}(\mathbf{x})$, and dynamical coordinates (p_c, q_c) strongly coupled to one material emitter oscillator of frequency ω_e, effective mass m, and dynamical coordinates (p_e, q_e) with strength $g_{pq}(\mathbf{s}) = -e\sqrt{4\pi/mV}\mathbf{f}(\mathbf{s}) \cdot \hat{\mathbf{q}}_e$. Note that the Newton equations in Equation 1 describing a weakly coupled emitter–cavity system are also derivable from Equation 24 but must be supplemented with phenomenological velocity-dependent frictional forces to account for the effects of radiative and nonradiative damping. It is also interesting to note that the inverse of the cavity mode volume V plays the role of an effective mass for the cavity, as seen in Equation 24. In the strong coupling regime in which environmental losses can be neglected, the above Hamiltonian (Equation 24), when quantized in the canonical manner such that $[\hat{q}_c, \hat{p}_c] = i\hbar$ and $[\hat{q}_e, \hat{p}_e] = i\hbar$ (98), serves as the starting point for a hierarchy of quantum optical Hamiltonians, including the celebrated Jaynes-Cummings and Tavis-Cummings models described below.

3.1. Jaynes-Cummings Model

The Jaynes-Cummings (JC) model (101) describes the interaction between a two-level system (TLS) and a single optical cavity mode. It derives from quantization of the light–matter Hamiltonian in Equation 24 together with replacement of the bosonic description of the matter with that of a TLS representing the ground $|g\rangle$ and excited $|e\rangle$ states of an emitter. By defining the dipole and electric field operators as $\hat{\mathbf{d}} = \hat{\mathbf{d}}^{(+)} + \hat{\mathbf{d}}^{(-)}$ and $\hat{\mathbf{E}} = \hat{\mathbf{E}}^{(+)} + \hat{\mathbf{E}}^{(-)}$, where $\hat{\mathbf{d}}^{(+)} = |e\rangle\langle e|\hat{\mathbf{d}}|g\rangle\langle g| = |e\rangle \mathbf{d}_{eg} \langle g|$, $\hat{\mathbf{E}}^{(+)}(\mathbf{x}) = i\sqrt{2\pi\hbar\omega_c/V}\mathbf{f}(\mathbf{x})\hat{a}e^{-i\phi}$, $\hat{\mathbf{d}}^{(-)} = [\hat{\mathbf{d}}^{(+)}]^\dagger$, and $\hat{\mathbf{E}}^{(-)} = [\hat{\mathbf{E}}^{(+)}]^\dagger$, the light–matter Hamiltonian becomes

$$\begin{aligned} \hat{H} &= \hbar\omega_c \hat{a}^\dagger \hat{a} + \hbar\omega_e \hat{\sigma}_+ \hat{\sigma}_- - \hat{\mathbf{E}}(\mathbf{s}) \cdot \hat{\mathbf{d}} \\ &= \hbar\omega_c \hat{a}^\dagger \hat{a} + \hbar\omega_e \hat{\sigma}_+ \hat{\sigma}_- + \underbrace{\left[-\hat{\mathbf{E}}^{(+)}(\mathbf{s}) \cdot \hat{\mathbf{d}}^{(+)} - \hat{\mathbf{E}}^{(-)}(\mathbf{s}) \cdot \hat{\mathbf{d}}^{(-)}\right]}_{\hat{H}_{\text{int}}^{(\text{res})}} + \underbrace{\left[-\hat{\mathbf{E}}^{(+)}(\mathbf{s}) \cdot \hat{\mathbf{d}}^{(-)} - \hat{\mathbf{E}}^{(-)}(\mathbf{s}) \cdot \hat{\mathbf{d}}^{(+)}\right]}_{\hat{H}_{\text{int}}^{(\text{antires})}} \end{aligned} \qquad 25.$$

in terms of the TLS excitation and deexcitation operators $\hat{\sigma}_+ = |e\rangle\langle g|$ and $\hat{\sigma}_- = |g\rangle\langle e|$. Expressed in the interaction picture, the antiresonant and resonant interactions

$$\begin{aligned}\hat{H}_{\text{int}}^{(\text{res})}(t) &= -\hat{\mathbf{E}}^{(+)}(\mathbf{s})\cdot\mathbf{d}_{eg}\hat{\sigma}_+ - \hat{\mathbf{E}}^{(-)}(\mathbf{s})\cdot\mathbf{d}_{ge}\hat{\sigma}_- \\ &= -i\hbar\underbrace{\left[\sqrt{\frac{2\pi\hbar\omega_c}{V}}\frac{\mathbf{f}(\mathbf{s})\cdot\mathbf{d}_{eg}}{\hbar}\right]}_{g} e^{-i(\omega_c-\omega_e)t}\hat{a}e^{-i\phi}\hat{\sigma}_+ + \text{H.c.}, \\ \hat{H}_{\text{int}}^{(\text{antires})}(t) &= -\hat{\mathbf{E}}^{(+)}(\mathbf{s})\cdot\mathbf{d}_{ge}\hat{\sigma}_- - \hat{\mathbf{E}}^{(-)}(\mathbf{s})\cdot\mathbf{d}_{eg}\hat{\sigma}_+ \\ &= -i\hbar\underbrace{\left[\sqrt{\frac{2\pi\hbar\omega_c}{V}}\frac{\mathbf{f}(\mathbf{s})\cdot\mathbf{d}_{ge}}{\hbar}\right]}_{\bar{g}} e^{-i(\omega_c+\omega_e)t}\hat{a}e^{-i\phi}\hat{\sigma}_- + \text{H.c.}\end{aligned} \quad 26.$$

are characterized by phase factors $e^{-i(\omega_c-\omega_e)t}$ and $e^{-i(\omega_c+\omega_e)t}$, with the former (energy-conserving) phase oscillating slowly while the latter (non-energy-conserving) phase oscillates rapidly when the cavity-emitter detuning $\delta = \omega_c - \omega_e$ is small (using the convention that $\omega_g = 0$). Under the RWA, the latter is neglected completely, resulting in the JC Hamiltonian

$$\hat{H}_{\text{JC}} = \hbar\omega_c\hat{a}^\dagger\hat{a} + \hbar\omega_e\hat{\sigma}_+\hat{\sigma}_- + \hbar g\hat{a}\hat{\sigma}_+ + \hbar g^*\hat{a}^\dagger\hat{\sigma}_- \quad 27.$$

in the Schrödinger picture, after choosing the arbitrary phase angle $\phi = -\pi/2$. Due to the TLS's limited state space of ground ($|g\rangle$) and excited ($|e\rangle$), only $|g,n\rangle$ and $|e,n-1\rangle$ states become coupled through $\hat{H}_{\text{int}}^{(\text{res})}$, and the Fock state representation of the JC Hamiltonian decomposes into 2×2 subspaces with n total excitations

$$\hat{H}_{\text{JC},n} = (n+1)\hbar\omega_c\begin{bmatrix}1 & 0\\ 0 & 1\end{bmatrix} + \hbar\begin{bmatrix}0 & g^*\sqrt{n}\\ g\sqrt{n} & -\delta\end{bmatrix} \quad 28.$$

expressed in terms of the cavity-emitter detuning δ. The energy levels and eigenstates within the nth manifold are

$$E_{n\pm} = n\hbar\omega_c - \frac{\hbar\delta}{2} \pm \frac{\hbar}{2}\sqrt{\delta^2 + 4|g|^2 n}, \quad 29.$$

$$|+,n\rangle = \cos\theta_n|e,n-1\rangle + \sin\theta_n|g,n\rangle,$$

$$|-,n\rangle = -\sin\theta_n|e,n-1\rangle + \cos\theta_n|g,n\rangle, \quad 30.$$

with coupling angle $\theta_n = (1/2)\tan^{-1}2\sqrt{n}|g|/(\omega_e-\omega_c)$ and splitting $E_{n+} - E_{n-} = \sqrt{n}\hbar\Omega$ at zero detuning defining the Rabi frequency $\Omega = 2|g| = 2\sqrt{2\pi\hbar\omega_c/V}|\mathbf{f}(\mathbf{s})\cdot\mathbf{d}_{eg}|/\hbar = 2|\mathbf{E}^{(+)}(\mathbf{s})\cdot\mathbf{d}_{eg}|/\hbar$ (102). The **Supplemental Material** offers an expanded discussion and generalization to N identical TLSs (the Tavis-Cummings model) with the inclusion of losses as well as a discussion of the ultrastrong coupling regime (USC), including the modification of the ground state composition and recent studies involving nanophotonic systems.

Supplemental Material >

3.2. Characterizing Strongly Coupled Systems

Many characteristics of strongly coupled systems have been studied with a broad range of molecular and solid-state emitters coupled to a variety of nanophotonic cavities (103–105). In particular, far-field optical spectroscopies have repeatedly verified the utility of Equation 29 (and its non-Hermitian analog) in describing the evolution of upper and lower polariton energies as system

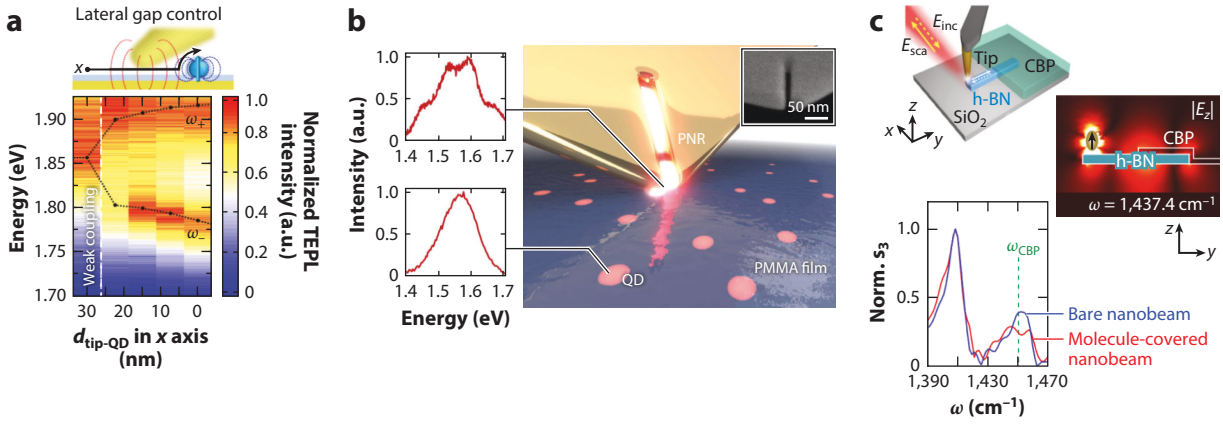

Figure 6

Probing strongly coupled systems with tip-enhanced measurements. (*a*) Reversible and dynamical interrogation of single CdSe/ZnS QDs in the strong coupling regime using TEPL spectroscopy. Panel adapted with permission from Reference 108; copyright 2019 Science. (*b*) Deterministic room temperature strong coupling of individual colloidal QDs to a plasmonic notch resonator at the tip of a scanning probe measured using TEPL. Panel adapted from Reference 109 (CC BY 4.0). (*c*) Nano-FTIR scheme, calculated spatial map of the model system response field, and measured amplitude spectra of the bare (*blue*) and molecule-covered (*red*) nanobeam. Upper and lower polaritons were observed in the amplitude spectra $S_3(\omega)$ of the combined system at frequencies above and below the uncoupled molecular vibration frequency ω_{CBP}. Panel adapted from Reference 110 (CC BY 4.0). Abbreviations: FTIR, Fourier transform infrared; PNR, plasmonic nanoresonator; QD, quantum dot; TEPL, tip-enhanced photoluminescence.

parameters are varied to tune the uncoupled mode energies as well as the $\sqrt{N}$ dependence of the Rabi splitting on the number of emitters coupled to the cavity (see **Supplemental Material**). An appreciation was also developed regarding the role played by the measurement observables in the determination of system parameters. For example, it was shown that Rabi splittings inferred from scattering measurements can be overestimated, and that it is therefore preferable to employ absorption or photoluminescence measurements to determine Rabi splitting energies (106, 107). Albeit in the weak coupling regime, References 31 and 30 independently came to the same conclusion in the quantification of Fano antiresonances in both optical and electron beam spectroscopies. Recent examples of TEPL measurements employing movable metallic tips to controllably and dynamically interrogate strong coupling to emitters are presented in **Figure 6**, with additional discussion provided in the **Supplemental Material**.

Supplemental Material >

In addition to the optical spectroscopies discussed thus far, free-electron-based measurements in scanning transmission electron microscopes (STEMs) have also provided unique access to the properties of nanophotonic structures and their detailed optical responses. Specifically, EEL spectroscopy, where the excitation spectrum of an interrogated sample is encoded in the difference in kinetic energy of a probing free electron before and after interaction, has been used for over a decade to spatially and spectrally map excitations of plasmonic (97, 116) as well as nanophotonic (75, 117) systems. Due to recent progress in monochromation and aberration correction technologies, $\lesssim$10 meV energy resolution is achievable in modern STEMs, opening the door to performing high-resolution spectroscopy of visible to far-infrared frequency excitations with spatial resolution ($\lesssim$1 nm) far below the optical diffraction limit (117–119). The **Supplemental Material** contains an expanded discussion of recent studies leveraging EEL spectroscopy and related techniques to probe strongly coupled nanophotonic systems, which are highlighted in **Figure 7**.

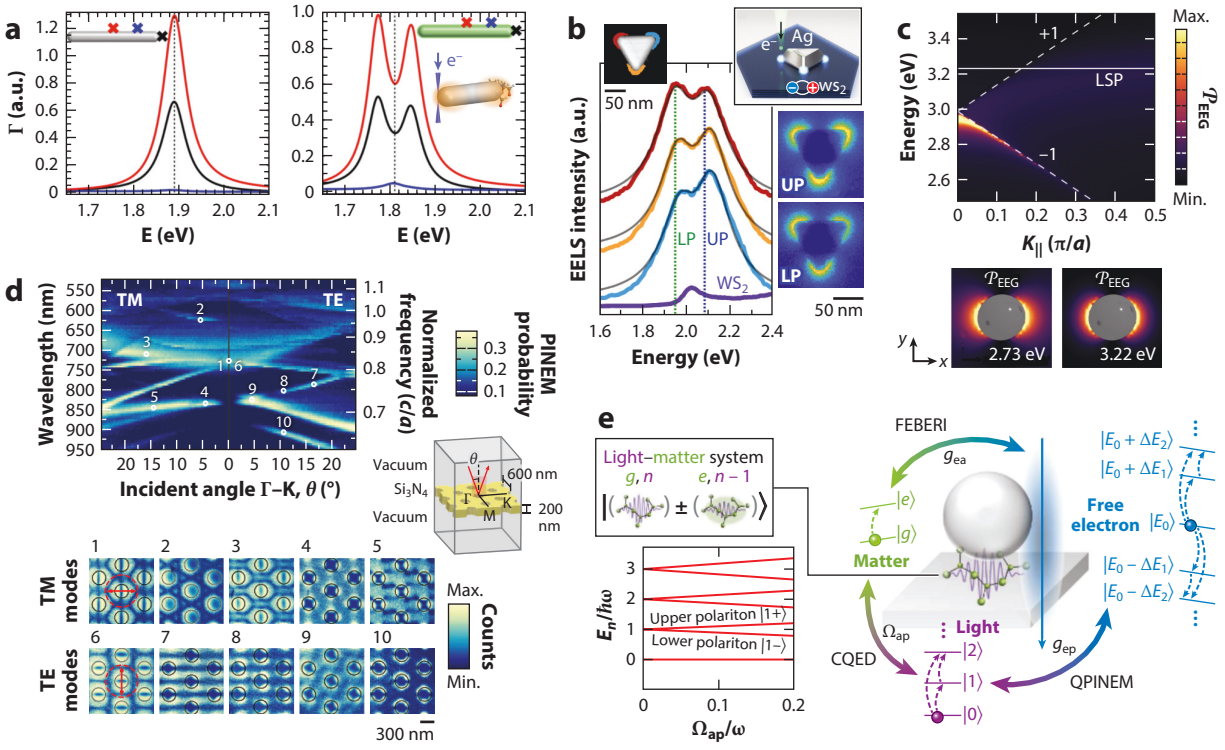

Figure 7

Probing strong coupling with free electrons. (*a*) Calculated EEL spectra of a bare Ag rod (*left*) and an Ag rod coated with an emitter medium shell (*right*) for various electron beam positions marked by color-coded crosses. Panel adapted with permission from Reference 111; copyright 2018 American Chemical Society. (*b*) Experimental spectral and spatial mapping of upper and lower polaritons using EEL spectroscopy for an Ag nanoprism coupled to WS_2 excitons at room temperature. Panel adapted with permission from Reference 112; copyright 2019 American Chemical Society. (*c*) Calculated EEG spectra of a one-dimensional plasmonic array structure as a function of the incident CW laser in-plane momentum $K_{\|}$, which encodes the array energy-momentum dispersion $E(k_{\|})$. Spatially resolved spectrum image calculations are presented at the upper and lower polariton energies for the same array structure embedded within a homogeneous slab of emitters. Panel adapted with permission from Reference 113; copyright 2022 American Physical Society. (*d*) Experimental measurement of Bloch mode $E(\mathbf{k}_{\|})$ dispersion in a photonic crystal using free electrons (*top*) and direct spectral mapping of Bloch modes in real space (*bottom*). Panel adapted with permission from Reference 114; copyright 2020 Springer Nature. (*e*) Coherent free electron probing of laser-stimulated light–matter targets in the strong coupling regime. Panel adapted with permission from Reference 115; copyright 2023 Science. Abbreviations: CW, continuous wave; EEG, electron energy gain; EEL, electron energy loss; LP, lower polariton; PINEM, photon-induced near-field electron microscopy; TE, transverse electric; TM, transverse magnetic; UP, upper polariton.

4. SUMMARY AND FUTURE OUTLOOK

Over half a century after the influential experiments of Purcell and Drexhage, today researchers have achieved an exquisite ability to tailor the interactions between light and matter through precision engineering of nanophotonic cavities capable of confining light to the nanoscopic dimensions of molecular, excitonic, phononic, and plasmonic excitations. Through weak coupling to nanophotonic cavities, exceedingly fragile optical processes have been enhanced to the point where the spectra of individual quantum objects can be resolved and investigated at room temperature with new levels of control, heralding separate renaissances in multiple fields of spectroscopy. In other contexts, entirely new states of emergent polaritonic matter have been coaxed into existence and

manipulated, sometimes actively, to realize novel strongly coupled optical phenomena that serve as playgrounds for exploration of quantum many-body physics.

In both weak and strong coupling regimes, the characterization of nanoscale material responses has been achieved using not only far-field optical measurements but also more sophisticated near-field optical and electron beam probes capable of simultaneously recording spectra and correlated images with spatial resolution below the diffraction limit of light. Owing to their ability to measure nanoscale optical processes at their native energy, length, momentum, time, and polarization scales, such near-field spectroscopies—or nanospectroscopies—represent some of the most information-rich observables available today, and, looking forward, we anticipate numerous future directions of inquiry that will benefit from the new limits of resolution that they offer.

Together with the nanospectroscopic measurements highlighted in this review comes the need for detailed theoretical modeling of the specific experimental observables being measured, as the observed spectra (and microscope images) often do not directly map to those of the isolated material excitation as is commonly assumed in many other molecular spectroscopies. This difference is due to the significance of interactions and losses shared between nanoscale material excitations and their local optical cavity environments as well as to the convolution of experimental signals by the specific response functions of the probes themselves. Said differently, the Hamiltonian eigenspectrum of the isolated material response is often a poor representation of the observed spectrum, and significant theoretical work is required to connect the two.

With these advances in cavity and emitter synthesis/fabrication, near- and far-field materials characterization, and theory, now is an exciting time for spectroscopists investigating the optical properties of individual, few, and ensembles of emitters coupled to nanophotonic cavity environments. Going forward, the future holds great promise for detailed explorations of cavity-enhanced optical processes at the nanoscale across varying interaction strengths and their associated physical regimes, opening new prospects for basic scientific research and the downstream technological applications that are enabled by it.

DISCLOSURE STATEMENT

The authors are not aware of any affiliations, memberships, funding, or financial holdings that might be perceived as affecting the objectivity of this review.

ACKNOWLEDGMENTS

We acknowledge support from the US National Science Foundation under awards CHE-1954393 and QII-TAQS-1936100, the US Department of Energy (DOE) Basic Energy Sciences (BES) under award DE-SC0022921 (to M.R.B., A.G.N., C.P.A., E.K.B., and D.J.M.), the US Department of Energy (DOE) Basic Energy Sciences (BES) under award DE-SC0021984 (to F.P. and J.A.D.), and the Center for Molecular Quantum Transduction, an Energy Frontier Research Center funded by DOE, Office of Science, BES, under award DE-SC0021314 (to R.H.G.).

LITERATURE CITED

1. Rayleigh L. 1910. The problem of the whispering gallery. *Philos. Mag.* 20(120):1001–4
2. Wise WH. 1929. Asymptotic dipole radiation formulas. *Bell Syst. Tech. J.* 8(4):662–71
3. Shelby RA, Smith DR, Schultz S. 2001. Experimental verification of a negative index of refraction. *Science* 292(5514):77–79
4. Pendry JB, Schurig D, Smith DR. 2006. Controlling electromagnetic fields. *Science* 312(5781):1780–82
5. Crommie M, Lutz C, Eigler D, Heller E. 1995. Quantum corrals. *Physica D* 83(1):98–108
6. Heller EJ. 1984. Bound-state eigenfunctions of classically chaotic Hamiltonian systems: scars of periodic orbits. *Phys. Rev. Lett.* 53(16):1515–18

7. Drexhage KH. 1966. *Optische Untersuchungen an neuartigen monomolekularen*. Habilitationsschr., Univ. Marburg, Ger.
8. Drexhage K. 1970. Influence of a dielectric interface on fluorescence decay time. *J. Lumin.* 1–2:693–701
9. Kuhn H. 2003. Classical aspects of energy transfer in molecular systems. *J. Chem. Phys.* 53(1):101–8
10. Chance RR, Prock A, Silbey R. 1978. Molecular fluorescence and energy transfer near interfaces. *Adv. Chem. Phys.* 37:1–65
11. Purcell EM. 1946. Spontaneous emission probabilities at radio frequencies. *Phys. Rev.* 69(11/12):674–81
12. Ritchie RH. 1957. Plasma losses by fast electrons in thin films. *Phys. Rev.* 106(5):874–81
13. Bohm D, Pines D. 1953. A collective description of electron interactions. III. Coulomb interactions in a degenerate electron gas. *Phys. Rev.* 92(3):609–25
14. Vahala KJ. 2003. Optical microcavities. *Nature* 424(6950):839–46
15. Wang P, Wang Y, Yang Z, Guo X, Lin X, et al. 2015. Single-band 2-nm-line-width plasmon resonance in a strongly coupled Au nanorod. *Nano Lett.* 15(11):7581–86
16. Wu Y, Hu Z, Kong XT, Idrobo JC, Nixon AG, et al. 2020. Infrared plasmonics: STEM-EELS characterization of Fabry-Pérot resonance damping in gold nanowires. *Phys. Rev. B* 101(8):085409
17. Barclay PE, Santori C, Fu KM, Beausoleil RG, Painter O. 2009. Coherent interference effects in a nano-assembled diamond NV center cavity-QED system. *Opt. Express* 17(10):8081–197
18. Rattenbacher D, Shkarin A, Renger J, Utikal T, Götzinger S, Sandoghdar V. 2019. Coherent coupling of single molecules to on-chip ring resonators. *New J. Phys.* 21(6):062002
19. Diddams SA, Vahala K, Udem T. 2020. Optical frequency combs: coherently uniting the electromagnetic spectrum. *Science* 369(6501):eaay3676
20. Nitzan A. 2006. *Chemical Dynamics in Condensed Phases*. Oxford, UK: Oxford Univ. Press
21. Cortes CL, Otten M, Gray SK. 2020. Non-Hermitian approach for quantum plasmonics. *J. Chem. Phys.* 152(8):084105
22. Novotny L, Hecht B. 2012. *Principles of Nano-Optics*. Cambridge, UK: Cambridge Univ. Press. 2nd ed.
23. Anger P, Bharadwaj P, Novotny L. 2006. Enhancement and quenching of single-molecule fluorescence. *Phys. Rev. Lett.* 96(11):113002
24. Munechika K, Chen Y, Tillack AF, Kulkarni AP, Jen-La Plante I, et al. 2011. Quantum dot/plasmonic nanoparticle metachromophores with quantum yields that vary with excitation wavelength. *Nano Lett.* 11(7):2725–30
25. ElKabbash M, Miele E, Fumani AK, Wolf MS, Bozzola A, et al. 2019. Cooperative energy transfer controls the spontaneous emission rate beyond field enhancement limits. *Phys. Rev. Lett.* 122(20):203901
26. Shahbazyan TV. 2016. Local density of states for nanoplasmonics. *Phys. Rev. Lett.* 117(20):207401
27. Shahbazyan TV. 2018. Spontaneous decay of a quantum emitter near a plasmonic nanostructure. *Phys. Rev. B* 98(11):115401
28. Bigelow NW, Vaschillo A, Camden JP, Masiello DJ. 2013. Signatures of Fano interferences in the electron energy loss spectroscopy and cathodoluminescence of symmetry-broken nanorod dimers. *ACS Nano* 7(5):4511–19
29. Thakkar N, Rea MT, Smith KC, Heylman KD, Quillin SC, et al. 2017. Sculpting Fano resonances to control photonic–plasmonic hybridization. *Nano Lett.* 17(11):6927–34
30. Smith KC, Olafsson A, Hu X, Quillin SC, Idrobo JC, et al. 2019. Direct observation of infrared plasmonic Fano antiresonances by a nanoscale electron probe. *Phys. Rev. Lett.* 123(17):177401
31. Pan F, Smith KC, Nguyen HL, Knapper KA, Masiello DJ, Goldsmith RH. 2019. Elucidating energy pathways through simultaneous measurement of absorption and transmission in a coupled plasmonic-photonic cavity. *Nano Lett.* 20(1):50–58
32. Luk'Yanchuk B, Zheludev NI, Maier SA, Halas NJ, Nordlander P, et al. 2010. The Fano resonance in plasmonic nanostructures and metamaterials. *Nat. Mater.* 9(9):707–15
33. Sheikholeslami SN, García-Etxarri A, Dionne JA. 2011. Controlling the interplay of electric and magnetic modes via Fano-like plasmon resonances. *Nano Lett.* 11(9):3927–34
34. Collins SM, Nicoletti O, Rossouw D, Ostasevicius T, Midgley PA. 2014. Excitation dependent Fano-like interference effects in plasmonic silver nanorods. *Phys. Rev. B* 90(15):155419
35. Dieringer JA, Wustholz KL, Masiello DJ, Camden JP, Kleinman SL, et al. 2009. Surface-enhanced Raman excitation spectroscopy of a single rhodamine 6G molecule. *J. Am. Chem. Soc.* 131(2):849–54

36. Camden JP, Dieringer JA, Wang Y, Masiello DJ, Marks LD, et al. 2008. Probing the structure of single-molecule surface-enhanced Raman scattering hot spots. *J. Am. Chem. Soc.* 130(38):12616–17
37. Jeanmaire DL, Van Duyne RP. 1977. Surface Raman spectroelectrochemistry. Part I: heterocyclic, aromatic, and aliphatic amines adsorbed on the anodized silver electrode. *J. Electroanal. Chem.* 84(1):1–20
38. Nie S, Emory SR. 1997. Probing single molecules and single nanoparticles by surface-enhanced Raman scattering. *Science* 275(5303):1102–6
39. Kneipp K, Wang Y, Kneipp H, Perelman LT, Itzkan I, et al. 1997. Single molecule detection using surface-enhanced Raman scattering (SERS). *Phys. Rev. Lett.* 78(9):1667–70
40. Leung PT, Liu SY, Young K. 1994. Completeness and orthogonality of quasinormal modes in leaky optical cavities. *Phys. Rev. A* 49(4):3057–67
41. Gérard JM. 2003. Solid-state cavity-quantum electrodynamics with self-assembled quantum dots. In *Single Quantum Dots: Fundamentals, Applications and New Concepts*, ed. P Michler, pp. 269–314. Berlin: Springer
42. Sauvan C, Hugonin JP, Maksymov IS, Lalanne P. 2013. Theory of the spontaneous optical emission of nanosize photonic and plasmon resonators. *Phys. Rev. Lett.* 110(23):237401
43. Kristensen PT, Hughes S. 2014. Modes and mode volumes of leaky optical cavities and plasmonic nanoresonators. *ACS Photon.* 1(1):2–10
44. Ren J, Franke S, Hughes S. 2021. Quasinormal modes, local density of states, and classical Purcell factors for coupled loss-gain resonators. *Phys. Rev. X* 11(4):041020
45. Sauvan C, Wu T, Zarouf R, Muljarov EA, Lalanne P. 2022. Normalization, orthogonality, and completeness of quasinormal modes of open systems: the case of electromagnetism [Invited]. *Opt. Express* 30(5):6846–85
46. Koenderink AF. 2010. On the use of Purcell factors for plasmon antennas. *Opt. Lett.* 35(24):4208–10
47. Jackson JD. 1999. *Classical Electrodynamics*. Hoboken, NJ: Wiley. 3rd ed.
48. Lassettre E, Krasnow M, Silverman S. 1964. Inelastic scattering of electrons by helium. *J. Chem. Phys.* 40(5):1242–48
49. Fano U. 1961. Effects of configuration interaction on intensities and phase shifts. *Phys. Rev.* 124(6):1866–78
50. Pan F, Karlsson K, Nixon AG, Hogan LT, Ward JM, et al. 2022. Active control of plasmonic–photonic interactions in a microbubble cavity. *J. Phys. Chem. C* 126(48):20470–79
51. Heylman KD, Thakkar N, Horak EH, Quillin SC, Cherqui C, et al. 2016. Optical microresonators as single-particle absorption spectrometers. *Nat. Photon.* 10(12):788–95
52. Doeleman HM, Verhagen E, Koenderink AF. 2016. Antenna–cavity hybrids: matching polar opposites for Purcell enhancements at any linewidth. *ACS Photon.* 3(10):1943–51
53. Frimmer M, Coenen T, Koenderink AF. 2012. Signature of a Fano resonance in a plasmonic metamolecule's local density of optical states. *Phys. Rev. Lett.* 108(7):077404
54. Losquin A, Kociak M. 2015. Link between cathodoluminescence and electron energy loss spectroscopy and the radiative and full electromagnetic local density of states. *ACS Photon.* 2(11):1619–27
55. Moerner WE, Kador L. 1989. Optical detection and spectroscopy of single molecules in a solid. *Phys. Rev. Lett.* 62(21):2535–38
56. Gaiduk A, Yorulmaz M, Ruijgrok PV, Orrit M. 2010. Room-temperature detection of a single molecule's absorption by photothermal contrast. *Science* 330(6002):353–56
57. Kukura P, Celebrano M, Renn A, Sandoghdar V. 2010. Single-molecule sensitivity in optical absorption at room temperature. *J. Phys. Chem. Lett.* 1(23):3323–27
58. Cognet L, Berciaud S, Lasne D, Lounis B. 2008. Photothermal methods for single nonluminescent nano-objects. *Anal. Chem.* 80(7):2288–94
59. Yorulmaz M, Nizzero S, Hoggard A, Wang LY, Cai YY, et al. 2015. Single-particle absorption spectroscopy by photothermal contrast. *Nano Lett.* 15(5):3041–47
60. Yorulmaz M, Hoggard A, Zhao H, Wen F, Chang WS, et al. 2016. Absorption spectroscopy of an individual Fano cluster. *Nano Lett.* 16(10):6497–503
61. Joplin A, Chang WS, Link S. 2018. Imaging and spectroscopy of single metal nanostructure absorption. *Langmuir* 34(13):3775–86

62. West CA, Lee SA, Shooter J, Searles EK, Goldwyn HJ, et al. 2023. Nonlinear effects in single-particle photothermal imaging. *J. Chem. Phys.* 158(2):024202
63. Heylman KD, Knapper KA, Goldsmith RH. 2014. Photothermal microscopy of nonluminescent single particles enabled by optical microresonators. *J. Phys. Chem. Lett.* 5(11):1917–23
64. Knapper KA, Heylman KD, Horak EH, Goldsmith RH. 2016. Chip-scale fabrication of high-Q all-glass toroidal microresonators for single-particle label-free imaging. *Adv. Mater.* 28(15):2945–50
65. Knapper KA, Pan F, Rea MT, Horak EH, Rogers JD, Goldsmith RH. 2018. Single-particle photothermal imaging via inverted excitation through high-Q all-glass toroidal microresonators. *Opt. Express* 26(19):25020–30
66. Hogan LT, Horak EH, Ward JM, Knapper KA, Nic Chormaic S, Goldsmith RH. 2019. Toward real-time monitoring and control of single nanoparticle properties with a microbubble resonator spectrometer. *ACS Nano* 13(11):12743–57
67. Horak EH, Rea MT, Heylman KD, Gelbwaser-Klimovsky D, Saikin SK, et al. 2018. Exploring electronic structure and order in polymers via single-particle microresonator spectroscopy. *Nano Lett.* 18(3):1600–7
68. Rea MT, Pan F, Horak EH, Knapper KA, Nguyen HL, et al. 2019. Investigating the mechanism of post-treatment on PEDOT/PSS via single-particle absorption spectroscopy. *J. Phys. Chem. C* 123(51):30781–90
69. Huang Q, Cunningham BT. 2019. Microcavity-mediated spectrally tunable amplification of absorption in plasmonic nanoantennas. *Nano Lett.* 19(8):5297–303
70. Ruesink F, Doeleman HM, Hendrikx R, Koenderink AF, Verhagen E. 2015. Perturbing open cavities: anomalous resonance frequency shifts in a hybrid cavity-nanoantenna system. *Phys. Rev. Lett.* 115(20):203904
71. Liu JN, Huang Q, Liu KK, Singamaneni S, Cunningham BT. 2017. Nanoantenna–microcavity hybrids with highly cooperative plasmonic–photonic coupling. *Nano Lett.* 17(12):7569–77
72. Ruesink F, Doeleman HM, Verhagen E, Koenderink AF. 2018. Controlling nanoantenna polarizability through backaction via a single cavity mode. *Phys. Rev. Lett.* 120(20):206101
73. Cognée KG, Doeleman HM, Lalanne P, Koenderink A. 2019. Cooperative interactions between nanoantennas in a high-Q cavity for unidirectional light sources. *Light Sci. Appl.* 8(1):115
74. Doeleman HM, Dieleman CD, Mennes C, Ehrler B, Koenderink AF. 2020. Observation of cooperative Purcell enhancements in antenna–cavity hybrids. *ACS Nano* 14(9):12027–36
75. Auad Y, Hamon C, Tencé M, Lourenço-Martins H, Mkhitaryan V, et al. 2021. Unveiling the coupling of single metallic nanoparticles to whispering-gallery microcavities. *Nano Lett.* 22(1):319–27
76. Liu C, Wu Y, Hu Z, Busche JA, Beutler EK, et al. 2019. Continuous wave resonant photon stimulated electron energy-gain and electron energy-loss spectroscopy of individual plasmonic nanoparticles. *ACS Photon.* 6(10):2499–508
77. Pelton M. 2015. Modified spontaneous emission in nanophotonic structures. *Nat. Photon.* 9(7):427–35
78. Fleischmann M, Hendra PJ, McQuillan AJ. 1974. Raman spectra of pyridine adsorbed at a silver electrode. *Chem. Phys. Lett.* 26(2):163–66
79. Albrecht MG, Creighton JA. 1977. Anomalously intense Raman spectra of pyridine at a silver electrode. *J. Am. Chem. Soc.* 99(15):5215–17
80. Moskovits M. 1978. Surface roughness and the enhanced intensity of Raman scattering by molecules adsorbed on metals. *J. Chem. Phys.* 69(9):4159–61
81. Le Ru E, Etchegoin P. 2008. *Principles of Surface-Enhanced Raman Spectroscopy and Related Plasmonic Effects*. Amsterdam: Elsevier
82. Langer J, Jimenez de Aberasturi D, Aizpurua J, Alvarez-Puebla RA, Auguié B, et al. 2019. Present and future of surface-enhanced Raman scattering. *ACS Nano* 14(1):28–117
83. Roelli P, Galland C, Piro N, Kippenberg TJ. 2016. Molecular cavity optomechanics as a theory of plasmon-enhanced Raman scattering. *Nat. Nanotechnol.* 11(2):164–69
84. Schmidt MK, Esteban R, Benz F, Baumberg JJ, Aizpurua J. 2017. Linking classical and molecular optomechanics descriptions of SERS. *Faraday Discuss.* 205:31–65
85. Gersten J, Nitzan A. 1980. Electromagnetic theory of enhanced Raman scattering by molecules adsorbed on rough surfaces. *J. Chem. Phys.* 73(7):3023–37

86. Zhao, Jensen L, Schatz GC. 2006. Pyridine-Ag_{20} cluster: a model system for studying surface-enhanced Raman scattering. *J. Am. Chem. Soc.* 128(9):2911–19
87. Jensen L, Aikens CM, Schatz GC. 2008. Electronic structure methods for studying surface-enhanced Raman scattering. *Chem. Soc. Rev.* 37(5):1061–73
88. Masiello DJ, Schatz GC. 2008. Many-body theory of surface-enhanced Raman scattering. *Phys. Rev. A* 78(4):042505
89. Schmidt MK, Esteban R, González-Tudela A, Giedke G, Aizpurua J. 2016. Quantum mechanical description of Raman scattering from molecules in plasmonic cavities. *ACS Nano* 10(6):6291–98
90. Aspelmeyer M, Kippenberg TJ, Marquardt F. 2014. Cavity optomechanics. *Rev. Mod. Phys.* 86(4):1391–452
91. Benz F, Schmidt MK, Dreismann A, Chikkaraddy R, Zhang Y, et al. 2016. Single-molecule optomechanics in "picocavities." *Science* 354(6313):726–29
92. Zhang Y, Aizpurua J, Esteban R. 2020. Optomechanical collective effects in surface-enhanced Raman scattering from many molecules. *ACS Photon.* 7(7):1676–88
93. Xu Y, Hu H, Chen W, Suo P, Zhang Y, et al. 2022. Phononic cavity optomechanics of atomically thin crystal in plasmonic nanocavity. *ACS Nano* 16(8):12711–19
94. Mueller NS, Arul R, Jakob LA, Blunt MO, Földes T, et al. 2022. Collective mid-infrared vibrations in surface-enhanced Raman scattering. *Nano Lett.* 22(17):7254–60
95. Quillin SC, Cherqui C, Montoni NP, Li G, Camden JP, Masiello DJ. 2016. Imaging plasmon hybridization in metal nanoparticle aggregates with electron energy-loss spectroscopy. *J. Phys. Chem. C* 120(37):20852–59
96. Cherqui C, Bigelow NW, Vaschillo A, Goldwyn H, Masiello DJ. 2014. Combined tight-binding and numerical electrodynamics understanding of the STEM/EELS magneto-optical responses of aromatic plasmon-supporting metal oligomers. *ACS Photon.* 1(10):1013–24
97. Cherqui C, Thakkar N, Li G, Camden JP, Masiello DJ. 2016. Characterizing localized surface plasmons using electron energy-loss spectroscopy. *Annu. Rev. Phys. Chem.* 67:331–57
98. Cohen-Tannoudji C, Dupont-Roc J, Grynberg G. 1997. *Photons and Atoms: Introduction to Quantum Electrodynamics*. Hoboken, NJ: Wiley
99. Smith KC, Chen Y, Majumdar A, Masiello DJ. 2020. Active tuning of hybridized modes in a heterogeneous photonic molecule. *Phys. Rev. Appl.* 13(4):044041
100. Anyanwu CP, Pakeltis G, Rack PD, Masiello DJ. 2023. Nanoscale characterization of individual three-dimensional split ring resonator systems. *ACS Appl. Opt. Mater.* 1(2):607–14
101. Jaynes ET, Cummings FW. 1963. Comparison of quantum and semiclassical radiation theories with application to the beam maser. *Proc. IEEE* 51(1):89–109
102. Smith KC, Bhattacharya A, Masiello DJ. 2021. Exact *k*-body representation of the Jaynes-Cummings interaction in the dressed basis: insight into many-body phenomena with light. *Phys. Rev. A* 104(1):013707
103. Barnes B, García Vidal F, Aizpurua J. 2018. Special issue on "strong coupling of molecules to cavities." *ACS Photon.* 5(1):1
104. Hensen M, Heilpern T, Gray SK, Pfeiffer W. 2018. Strong coupling and entanglement of quantum emitters embedded in a nanoantenna-enhanced plasmonic cavity. *ACS Photon.* 5(1):240–48
105. Garcia-Vidal FJ, Ciuti C, Ebbesen TW. 2021. Manipulating matter by strong coupling to vacuum fields. *Science* 373(6551):eabd0336
106. Wersäll M, Cuadra J, Antosiewicz TJ, Balci S, Shegai T. 2017. Observation of mode splitting in photoluminescence of individual plasmonic nanoparticles strongly coupled to molecular excitons. *Nano Lett.* 17(1):551–58
107. Leng H, Szychowski B, Daniel MC, Pelton M. 2018. Strong coupling and induced transparency at room temperature with single quantum dots and gap plasmons. *Nat. Commun.* 9(1):4012
108. Park KD, May MA, Leng H, Wang J, Kropp JA, et al. 2019. Tip-enhanced strong coupling spectroscopy, imaging, and control of a single quantum emitter. *Sci. Adv.* 5(7):eaav5931
109. Groß H, Hamm JM, Tufarelli T, Hess O, Hecht B. 2018. Near-field strong coupling of single quantum dots. *Sci. Adv.* 4(3):eaar4906

110. Dolado I, Maciel-Escudero C, Nikulina E, Modin E, Calavalle F, et al. 2022. Remote near-field spectroscopy of vibrational strong coupling between organic molecules and phononic nanoresonators. *Nat. Commun.* 13(1):6850
111. Konečná A, Neuman T, Aizpurua J, Hillenbrand R. 2018. Surface-enhanced molecular electron energy loss spectroscopy. *ACS Nano* 12(5):4775–86
112. Yankovich AB, Munkhbat B, Baranov DG, Cuadra J, Olsén E, et al. 2019. Visualizing spatial variations of plasmon-exciton polaritons at the nanoscale using electron microscopy. *Nano Lett.* 19(11):8171–81
113. Bourgeois MR, Beutler EK, Khorasani S, Panek N, Masiello DJ. 2022. Nanometer-scale spatial and spectral mapping of exciton polaritons in structured plasmonic cavities. *Phys. Rev. Lett.* 128(19):197401
114. Wang K, Dahan R, Shentcis M, Kauffmann Y, Ben Hayun A, et al. 2020. Coherent interaction between free electrons and a photonic cavity. *Nature* 582(7810):50–54
115. Karnieli A, Tsesses S, Yu R, Rivera N, Zhao Z, et al. 2023. Quantum sensing of strongly coupled light-matter systems using free electrons. *Sci. Adv.* 9(1):eadd2349
116. Nelayah J, Kociak M, Stéphan O, García de Abajo FJ, Tencé M, et al. 2007. Mapping surface plasmons on a single metallic nanoparticle. *Nat. Phys.* 3(5):348–53
117. Polman A, Kociak M, García de Abajo FJ. 2019. Electron-beam spectroscopy for nanophotonics. *Nat. Mater.* 18(11):1158–71
118. Hachtel JA, Huang J, Popovs I, Jansone-Popova S, Keum JK, et al. 2019. Identification of site-specific isotopic labels by vibrational spectroscopy in the electron microscope. *Science* 363(6426):525–28
119. García de Abajo FJ, Di Giulio V. 2021. Optical excitations with electron beams: challenges and opportunities. *ACS Photon.* 8(4):945–74